Particle-laden exchange flows in inclined pipes

Nima Mirzaeian* and Kamran Alba
Department of Engineering Technology, University of Houston, Houston, Texas 77204, USA

(Received 3 May 2018; published 15 November 2018)

Lock-exchange suspension gravity current in a tilted narrow pipe is studied experimentally at very low Reynolds numbers. We investigate the interpenetration of a heavy particle-laden fluid on top of a light pure fluid by considering the effects of the initial volume fraction of particles ϕ_0 and inclination angle of the pipe from vertical β. Density mismatch between heavy and light phases is maintained low (Boussinesq limit) to allow a stable quasiparallel viscous flow. Pertaining to whether particles stay mixed in the suspension or sediment, three distinct mixing, transitionary, and sedimentary regimes are identified. Results of the classification over a wide range of particle concentration $\phi_0 \in [0.05,\ 0.50]$ and inclination angle $\beta \in [0^\circ,\ 88^\circ]$ are proposed in dimensionless phase diagrams suitable for industrial calculations. Mixing behavior emerges at sharp inclinations as flow continues steadily along the pipe. Sedimentary behavior is attributed to the decelerating flows that involve dilute or packed suspensions over nearly horizontal angles. To quantify the interpenetration rate, a scaling analysis is performed to approximate the velocity of the particle-laden front for different values of ϕ_0 and β. Furthermore, the impacts of the fluid's viscosity and particle size are investigated in detail. Reducing the particle size generally weakens the sedimentary behavior of the flow. Increasing the liquid's viscosity has almost no effect on regime transition, yet it results in slower advancing speed across all tilt angles.

DOI: 10.1103/PhysRevFluids.3.114301

I. INTRODUCTION

Buoyancy-driven interpenetrating flow of a heavy mixture into a light ambient occurs widely in oceanography, meteorology, and geophysics [1–3]. There are also multiple applications of these flows in the industry such as chemical, mining, and petroleum processes [4,5]. These multiphase flows have been vastly studied experimentally [6–8], analytically [9–12], and computationally [13–15] for pure fluids, i.e., in the absence of solid particles. In most practical situations, however, at least one of the involving fluids is particle-laden, therefore, not pure. Particulate flows have been studied in the literature primarily in the contexts of enhanced sedimentation in inclined pipes (Boycott flow) [16–18], turbidity currents [19,20], and debris flows over a substrate [21,22]. The interpenetrating exchange flow of a suspension into a pure fluid within a practical duct geometry still remains to be meticulously studied. The complexity of particle-laden currents arises from the effect that sedimentation imposes on the evolution of flow. Basically, settling tends to reduce the concentration of particles within the heavy mixture and ultimately the driving buoyancy force of the flow. Therefore, many of the interpenetrating velocity scales obtained by inertia-buoyancy [6,23] or viscous-buoyancy balance [7] in the case of pure fluids may no longer be applicable to suspension flows.

This study focuses on a context in literature related to particle-laden gravity currents, which occur in the presence of density gradient acting on both liquid and solid phases in the flow. The

*nima.mirzaeian@gmail.com

propagation of viscous particle-laden flows, when inertia is negligible, has been studied extensively considering a free-surface geometry. Previously, particle-laden thin film flows on inclined planes have been carefully investigated concentrating on relative particle motion in fluid [21], propagating front position [24], shear-induced migration [25], and phase separation [26]. The role of geometry confinement in the sedimentary systems was first investigated for channels with small [16,17] and large aspect ratios [18,27]. These works revealed that the purified fluid due to sedimentation can be convected through a clarified layer enhancing the settling process in inclined geometries. While flow dynamics within a *single* suspension mixture in duct geometry is studied well in the literature, solid-fluid interactions in a system composed practically of *two* mixtures is a new topic [28]. One of the recent relevant studies is the experimental work of Saha *et al.* (2013) on suspension exchange flow in horizontal Hele-Shaw channels [28]. They found that the particle-laden layer undergoes a sedimentary phase and finally halts at a finite distance. See also Ref. [29] for our most recent work theoretically studying suspension exchange flows via frontal shape and advancement speeds in a vertical duct.

The novelty of the present work is in extending the study of Saha *et al.* (2013) [28] carried for horizontal ducts by including the important effect of inclination angle as well as accounting for a full range of particle concentration from dilute to packed limits. Various regimes observed experimentally at low Reynolds number are classified in dimensionless maps suitable for industrial design. Moreover, the advancing speed of the suspension layer into the light ambient is quantified over a wide range of flow parameters. Numerous applications of such flows are found through the discharge, transport and dispersion of slurries, mine tailings, pastes, pharmaceuticals, paper pulp, drill cuttings, sludge, effluents and sewage [30–32], manufacture of cement clinker in inclined kilns [33], mineral processing in hydrocyclones [34], and inclined fluidized beds [35].

After discussing the experimental methodology and parameters in Sec. II, main features of buoyancy-driven exchange flow in inclined pipes will be briefly explained in Sec. III A. Particle-laden exchange flow is first discussed in Sec. III B for near-horizontal pipe. Subsequently, various flow regimes that emerge upon tilting the pipe will be introduced in Sec. III C 1. Analyses of effects of particle size and liquid's viscosity will be given in Secs. III C 2 and III C 3, respectively. Finally, the paper closes with a brief summary in Sec. IV.

II. EXPERIMENTAL APPROACH

A. Methodology

We utilize an experimental apparatus consisting of an acrylic pipe with a pneumatic gate valve in the middle as shown in Fig 1. The inner diameter and total length of the pipe are $\hat{D} = 9.53\,\text{mm}$ and $\hat{L} = 2000\,\text{mm}$, respectively. These dimensions result in a small aspect ratio ($\delta = \hat{D}/\hat{L} \approx 0.0048$) suitable for capturing the long time and fully developed effects of the flow [28,29,36]. The entire visible pipe section is mounted on an aluminum frame which allows tilting of the pipe in the clockwise way at an angle of inclination β, measured from the vertical direction. Heavy suspension occupies the left-hand side of the pipe, and light pure fluid the right-hand side. To maintain a *lock-exchange* configuration, shut-off valves at two ends of the system are closed immediately after heavy and light fluids are in place. At $\hat{t} = 0$, the gate valve is opened allowing heavy particle-laden mixture to penetrate into the pure liquid ambient. The experiment continues until the heavy front reaches the opposite end of the pipe or halts at a run-out distance; whichever occurs first. As depicted in the Fig. 1, the suspension is constantly mixed in the bucket, and at the same time, circulating through a robust flow transport system (via pumps and solenoid valves) to avoid premature settling or any inhomogeneity. Besides, the density and temperature of the mixture are properly monitored, recorded, and controlled to minimize the error in the initial particle concentration values ϕ_0. With this procedure, the resting time of the mixture in the pipe before the start of the experiment is maintained below 10 s which is negligible compared to the sedimenting time of suspension (∼20–1800 min). Therefore, there is almost no chance for particles to sediment before the release of the gate.

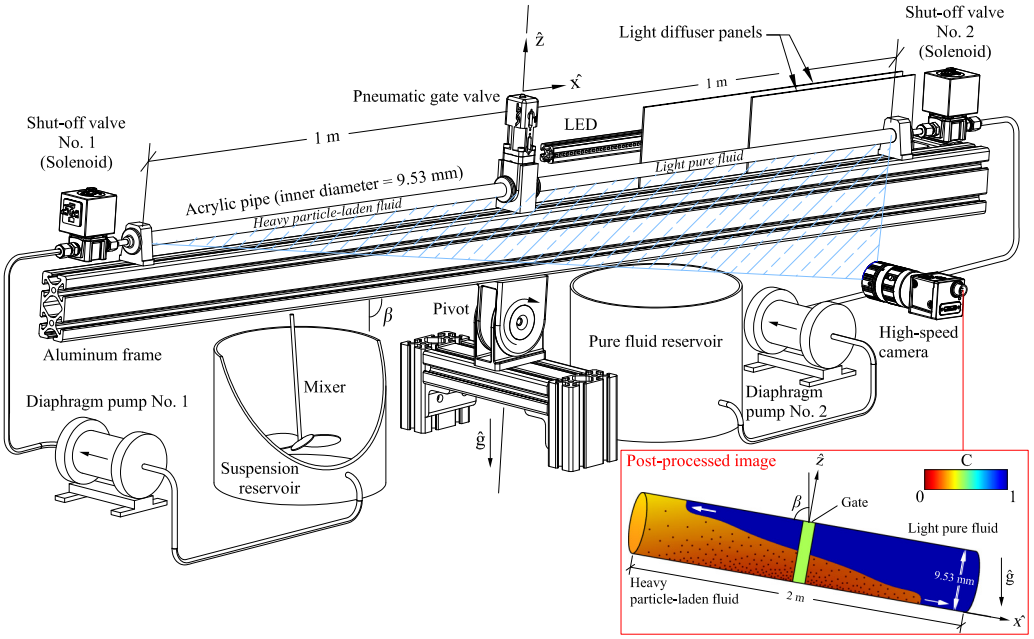

FIG. 1. Schematic of the experimental apparatus. The entire system can be tilted at an angle, β, measured from the vertical direction. The interface shape and particle distribution in the bottom right image are illustrative only.

The pipe is illuminated by placing light-emitting diode (LED) strips behind two light-diffusing panels to obtain a homogeneous lightening. Images are taken every 0.5 s using a high-speed camera (Basler Ace acA2040-90um CMOS, 2048^2 pixels) positioned at an adequately far location from the pipe. Once images are recorded, the concentration values $C(\hat{x}, \hat{z}, \hat{t})$ are calculated from the light intensity of each pixel according to the Beer-Lambert law by assuming an exponential dependency of the light intensity I, on concentration as $I(C) = \Gamma \exp(\alpha C)$; here, Γ and α are physical constants determined through calibration [37]. The incoming light intensity might slightly vary across the width of the pipe because of its curvature. Around the center of the pipe where there is a larger depth of the well-mixed suspension hindering the backlight, the picture may look more opaque than the areas near walls where depth is not as large. To mitigate this effect, we carefully record two reference images for each experiment, one dark and one light, by filling the entire pipe once with suspension and then with pure fluid, respectively. Regardless of the illumination condition, this procedure enables us to ensure that each pixel takes an accurate concentration value between 0 and 1, corresponding to suspension and pure fluid, respectively. Nevertheless, particle sedimentation tends to decrease the local concentration $C(\hat{x}, \hat{z}, \hat{t})$ to values less than 0 considered for the well-mixed suspension at the beginning of the experiment. In fact, particles can agglomerate to the extent that no light can practically pass through the sediment layer, plunging down the local concentration to negative values. To avoid uncontrollable and inconsistent variations in concentration profile we assigned 0 to negative values of C in our image processing algorithm for all experiments. Moreover, it is observed that the sediment layer (supposedly with negative C value) is considerably thin and with no significant impact on the spreading of fronts. Therefore, adjusting the negative concentration values in the explained manner has no major physical ramifications. These adjustments in the concentration domain enables us to define the frontal position and speed reliably across all the experiments; see Sec. III B for details. A schematic post-processed image of the pipe with scaled light intensity is presented in the inset of Fig. 1.

TABLE I. List of *dimensional* independent parameters in the experiments.

Definition	Parameter	Range
Gravitational acceleration	$\hat{g}$	$9.81\,\mathrm{m\,s^{-2}}$
Pipe diameter	$\hat{D}$	9.53 mm
Pipe length	$\hat{L}$	2 m
Particle diameter	$\hat{d}$	40, 70 μm[a]
Particle density	$\hat{\rho}_p$	$2500\,\mathrm{kg\,m^{-3}}$
Pure fluid density	$\hat{\rho}_f$	$1243.0, 1253.4\,\mathrm{kg\,m^{-3}}$
Pure fluid viscosity	$\hat{\mu}_f$	0.367, 0.765 Pa s
Initial volume of particles	$\hat{V}_p$	$3.56\text{-}35.59\,\mathrm{cm^3}$
Jamming volume of particles	$\hat{V}_j$	$47.69\,\mathrm{cm^3}$

[a]Mean particle diameters for two sets with D50 distribution: (1) $\hat{d} \in [35, 45]$ μm, (2) $\hat{d} \in [65, 75]$ μm. The majority of experiments are performed using $\hat{d} = 70$ μm.

B. Range of parameters

Consistent with our recent theoretical work on the same topic [29], our experiments involve nine independent *dimensional* parameters which we henceforth denote with a circumflex (ˆ). The gravitational acceleration is denoted by $\hat{g}$, pipe diameter $\hat{D}$, and pipe length $\hat{L}$. Solid particles have density $\hat{\rho}_p$. The particles diameter, $\hat{d}$, is adequately large for suspension to be *non-Brownian* [38], whereas, it is relatively small compared to the pipe diameter, i.e., $1\ \mu\mathrm{m} \ll \hat{d} \ll \hat{D}$. Density and viscosity of carrying fluid (the same as light pure fluid) are $\hat{\rho}_f$, and $\hat{\mu}_f$, accordingly. Initial and jamming volume of particles are $\hat{V}_p$ and $\hat{V}_j$, respectively. The latter depends on the shape and packing arrangement of particles [28]. A total of seven independent *dimensionless* controlling parameters are evaluated [29], namely, pipe aspect ratio, $\delta = \hat{D}/\hat{L} \ll 1$, angle of inclination β, particle-to-pipe-diameter ratio $r_p = \hat{d}/\hat{D} \ll 1$, particle-to-fluid-density ratio $\xi = \hat{\rho}_p/\hat{\rho}_f$, initial volume fraction of particles $\phi_0 = \hat{V}_p/\hat{V}_H$, jamming volume fraction $\phi_j = \hat{V}_j/\hat{V}_H$, and Reynolds number $\mathrm{Re}_t = \hat{\rho}_H(\phi_0)\hat{V}_t\hat{D}/\hat{\mu}_H(\phi_0)$. Assuming that the suspension solution initially fills half of the pipe, the volume of the heavy solution, $\hat{V}_H$, is approximated as $\hat{V}_H = \pi\hat{D}^2\hat{L}/8$. The density of the suspension is expressed as $\hat{\rho}_H(\phi_0) = \hat{\rho}_p\phi_0 + \hat{\rho}_f(1-\phi_0)$. The viscosity of the suspension may be captured via a Newtonian rheology in the form of $\hat{\mu}_H(\phi_0) = \hat{\mu}_f(1-\phi_0/\phi_j)^{-2}$ [39], in which, jamming volume fraction for spherical particles is proposed as $\phi_j \approx 0.61$ [28,40]. The characteristic velocity, $\hat{V}_t$, in the Reynolds number expression is given by Eq. (1); see also Ref. [37]. The dimensional and dimensionless parameters governing the flow along with their range and values are listed in Tables I and II, respectively. These parameters are also conveniently provided in captions of the figures throughout this paper.

Suspension in our experiments consists of negatively buoyant solid particles and a pure Newtonian carrying fluid with the same viscosity and density as the light pure fluid. Our choices of particles are two different sizes of soda-lime glass microspheres (Cospheric LLC) with density $\hat{\rho}_p = 2500 \pm 50\,\mathrm{kg\,m^{-3}}$. The first type involves smooth spheres with mean diameter 70 μm. The calculated standard deviation of a D50 Gaussian distribution for the range [65, 75] μm, i.e., 50% are between 65 and 75, is approximately 7 μm. The second type has a mean diameter of 40 μm with a similar distribution. Particles are suspended within two different aqueous glycerin solutions, one with 93% glycerin-water concentration by weight with density $\hat{\rho}_f = 1243.0 \pm 0.1\,\mathrm{kg\,m^{-3}}$ and viscosity $\hat{\mu}_f = 0.367 \pm 0.001$ Pa s, another one is a 97% glycerin-water solution with density $\hat{\rho}_f = 1253.4 \pm 0.1\,\mathrm{kg\,m^{-3}}$ and viscosity $\hat{\mu}_f = 0.765 \pm 0.001$ Pa s. We consider the same values for viscosity as reported in Ref. [41]. The density and temperature of the glycerin-water solution were controlled by an Anton Paar DMA 35 portable density meter (resolution, $0.0001\,\mathrm{g/cm^3}$). A portion of the solution was then weighed and transferred into a different container for preparing the

TABLE II. List of *dimensionless* independent parameters in the experiments.

Definition	Parameter	Range
Aspect ratio	$\delta = \frac{\hat{D}}{\hat{L}}$	4.8×10^{-3}
Pipe inclination angle	β	$0^\circ - 88^\circ$
Particle-to-pipe-diameter ratio	$r_p = \frac{\hat{d}}{\hat{D}}$	0.004, 0.007
Particle-to-fluid density ratio	$\xi = \frac{\hat{\rho}_p}{\hat{\rho}_f}$	1.99, 2.01
Initial volume fraction of particles	$\phi_0 = \frac{\hat{V}_p}{\hat{V}_H}$ [a]	0.05–0.50
Jamming volume fraction of particles	$\phi_j = \frac{\hat{V}_j}{\hat{V}_H}$	≈ 0.61 [b]
Reynolds number	$\mathrm{Re}_t = \frac{\hat{\rho}_H(\phi_0)\hat{V}_t\hat{D}}{\hat{\mu}_H(\phi_0)}$ [c]	0.10-1.72

[a]Initial volume of heavy fluid is approximately $\hat{V}_H = \pi \hat{D}^2 \hat{L}/8$.
[b]As reported in Ref. [28].
[c]Characteristic velocity given by Eq. (1).

suspension. Particles were stored in a dry container to avoid introducing moisture and contamination into the suspension. Suspension was prepared by weighting particles on a precision scale (resolution, 0.1 g), pouring fluid first in a reservoir agitated by a heavy-duty mixer (IKA Eurostar 200), and at the end adding particles continuously but slowly. This procedure ensures maintaining a uniform and bubble-free mixture. To examine the accuracy of initial particle concentration after adding particles, we measured the densities of at least three samples of the mixture using a density meter (Attension Sigma 701) with 0.1 kg m^{-3} resolution, and successfully verified the results with theory, $\hat{\rho}_H(\phi) = \hat{\rho}_p\phi_0 + \hat{\rho}_f(1-\phi_0)$ [28]. The error in recorded densities was reported as 5 kg m^{-3} which is equivalent to negligible 0.01 difference in obtained ϕ_0. Highly exothermic mixing was experienced due to the extreme shear forces inflicted by the mixer propeller on the bulk of the viscous mixture. Therefore, for avoiding uncontrolled temperature variations (and consequently changes in density and viscosity), we immersed the mixing chamber in a cold-water bath. Under this controlled condition, temperature always remained in the limit of $291 \sim 294$ K (measured by OMEGAETTE HH308 thermometer with, resolution, ± 0.1 K). Moreover, β is measured by an angle indicator with $\pm 0.1^\circ$ resolution.

Three separate sets of experiments were designed all with $\beta \in [0^\circ - 88^\circ]$. First, set A includes 47 experiments involving particle size $\hat{d} = 70\,\mu$m, and initial volume fractions $\phi_0 = \{0.05, 0.15, 0.30, 0.40, 0.50\}$. Particles are suspended in the less viscous 93 wt% aqueous glycerin solution. For investigating the effect of particle size, we consider the fluid in set B being the same as set A, while using smaller particles $\hat{d} = 40\,\mu$m, with initial volume fractions $\phi_0 = \{0.05, 0.30, 0.50\}$ (21 experiments). For set C, we consider the more viscous 97 wt% solution. This set also consists of 21 experiments, designed to study the effect of interstitial fluid on the flow. Table III lists three sets of experiments and their assigned variables.

TABLE III. List of experimental sets along with their ranges of parameters.

	$\hat{d}$ (μm)	$\hat{\mu}_f$ (Pa s)	$\hat{\rho}_f$ (kg m^{-3})	$\hat{u}_0$ [a] (mm s^{-1})	r_p	ξ
Set A	70	0.367	1243.0	0.009	0.007	2.01
Set B	40	0.367	1243.0	0.003	0.004	2.01
Set C	70	0.765	1253.4	0.004	0.007	1.99

[a]Stokes settling velocity $\hat{u}_0 = (\hat{\rho}_p - \hat{\rho}_f)\hat{g}\hat{d}^2/(18\hat{\mu}_f)$ [28].

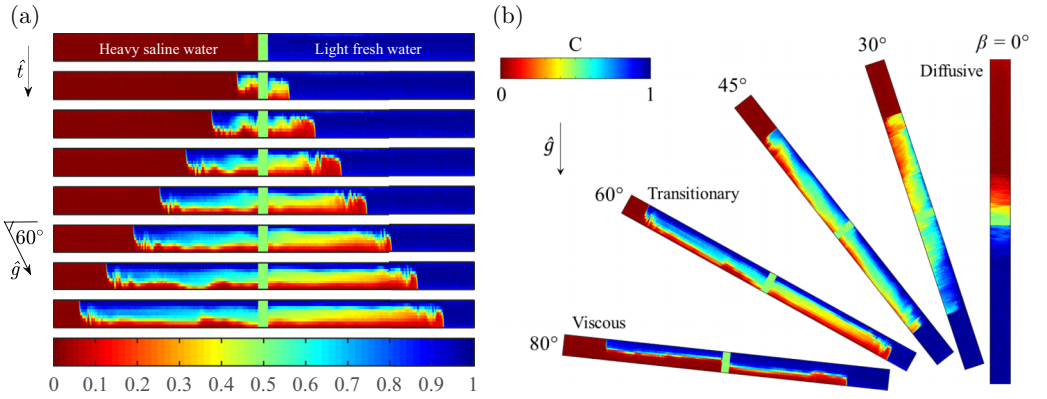

FIG. 2. (a) Sequence of experimental images for pure exchange flow obtained for $\beta = 60^\circ$ at times $\hat{t} = [0, 5, 11, \ldots 32, 37]$ s with $\hat{\rho}_H = 1018.4\,\mathrm{kg\,m^{-3}}$, $\hat{\rho}_L = 998.1\,\mathrm{kg\,m^{-3}}$, and $\hat{\mu}_H = \hat{\mu}_L = 1 \times 10^{-3}$ Pa s (At = 0.01 [Atwood number, $\mathrm{At} = (\hat{\rho}_H - \hat{\rho}_L)/(\hat{\rho}_H + \hat{\rho}_L)$], $\phi_0 = 0$, $\mathrm{Re}_t = 291$, $\xi = 0$, and $r_p = 0$). (b) Array of images over the full range of inclination angle, β, at $\hat{t} \approx 35$ s. The field of view is $2000 \times 9.53\,\mathrm{mm}^2$ in all the images. The color bar at the top left of the figure shows concentration value C, with 0 and 1 referring to the pure heavy and light fluids, respectively.

III. RESULTS

A. Buoyancy-driven exchange flow of pure fluids in inclined pipes

Before proceeding to the particle-laden limit, we first performed 33 experiments with pure mixtures to (1) Explore the effect of buoyant mixing in the absence of particles to provide a basis for comparison with further suspension experiments. (2) Validate our experimental apparatus through benchmarking against the well-established results of Seon *et al.* (2005) and (2007), obtained for various density contrasts and tilt angles [6,23]. Two major effects are observed as seen in Fig. 2(a). First, interpenetration in the form of quasiparallel layers of heavy fluid, named *leading*, into the light pure one, termed as *trailing* over time is evident. Second, at angles away from horizontal, transverse mixing, in the form of Kevin-Helmholtz instabilities, homogenizes local density contrast at the interface [6]. The depth-averaged concentration value $\bar{C}(\hat{x}, \hat{t})$ is simply the mean value of the fluid concentration averaged across the pipe at location $\hat{x}$ and time $\hat{t}$ and can be used to estimate the degree of mixing inside the pipe, or the height of the fluid when there is no mixing [8,36]. Similar to Seon *et al.* (2005) [6], we observed three different flow regimes by increasing β, i.e., decreasing inclination [Fig. 2(b)]. (I) *diffusive*: for pipes close to vertical, flow is turbulent and thoroughly diffusive meaning that the averaged concentration profile $\bar{C}(\hat{x}, \hat{t})$ follows a macroscopic diffusion law which is shown in our Appendix; see also Ref. [23]. (II) *Transitionary*: by further increasing β, mixing across the width of the pipe becomes weaker, and $\bar{C}(\hat{x}, \hat{t})$ no longer follows the diffusive law [6,23]. Inertia is the dominant limiting process during the first and second flow regimes. (III) *Viscous*: finally, heavy and light fronts steadily evolve over time in the form of separated counter-current layers with minimal transverse mixing. Flow in this regime is controlled by viscous-buoyant stress balance. Seon *et al.* (2007) have shown in viscous regime except the particular case of horizontal pipe, the front always reaches a constant velocity [23]. Thus, in the following section, the special case of $\beta = 90^\circ$ is excluded from our experiments for generality. See the Appendix for quantitative classification of different flow regimes and benchmarking results.

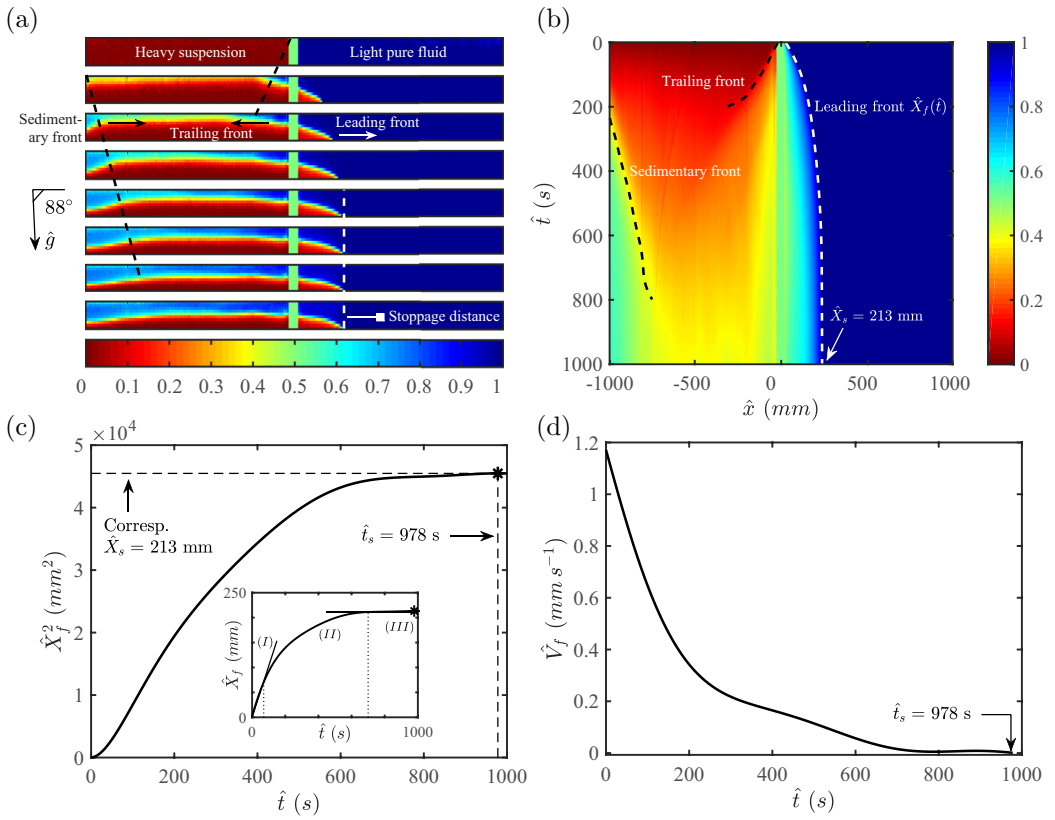

FIG. 3. (a) Sequence of images at times $\hat{t} = [0, 136, 272, \ldots 816, 952]$ s—the field of view is $2000 \times 9.53\,\text{mm}^2$, (b) spatiotemporal diagram of the depth-averaged concentration, (c) leading front's location with time, and (d) frontal velocity dependency on time for a particle-laden exchange experiment from set A: $\phi_0 = 0.30$, $\beta = 88^\circ$, $\hat{d} = 70\ \mu$m, $\hat{\mu}_f = 0.367$ Pa s, and $\hat{u}_0 = 0.009\,\text{mm s}^{-1}$ ($\psi = 0.767$, $\text{Re}_t = 1.21$, $\xi = 2.01$, and $r_p = 0.007$). Stoppage time and distance in part (c) are denoted by $\hat{t}_s$ and $\hat{X}_s$, respectively. Dashed lines in parts (a) and (b) mark the proximate locations of leading, trailing and sedimentary fronts over time; arrows show relative directions. Labels (I), (II), and (III) in the inset of part (c) correspond to inertia, viscous, and sedimentary phases, respectively.

B. Particle-laden exchange flows in near-horizontal angles: Halt time and distance

Unlike interpenetrating flow of pure fluids in which buoyancy forces arise from the density difference between heavy fluid and light ambient (using salt), such forces in suspension gravity currents originate from denser particles in the mixture [28]. In near-horizontal pipes, upon releasing the gate, similar exchanging *leading* and *trailing* fronts are formed [see Fig. 3(a)]. The settling of particles away from the downward-facing wall (surface) of the pipe is also conspicuous. Due to the depthwise settling, trailing front created by light pure fluid disappears after a while [see third to fifth snapshots in Fig. 3(a)]. The disappearance of the trailing front is accompanied by the formation of a *sedimentary* front on the very left-hand side of the tube marked in Fig. 3(a). When there is no significant mixing across the pipe, the depth-averaged concentration profile $\bar{C}(\hat{x}, \hat{t})$ can be used to estimate the interface height at any distance $\hat{x}$. Location of the leading, trailing, and sedimentary fronts at any time $\hat{t}$, are obtainable from $\bar{C}(\hat{x}, \hat{t})$, where the height of the interface is 5%, 95%, and 40% of the pipe diameter, respectively [42]. It should be mentioned that the usage of ninth-degree polynomials for curve-fitting of the experimental data has resulted in the accurate, smooth, continuous, and thus differentiable functions that can be used to conveniently estimate the

frontal displacement and velocity. Results are displayed in spatiotemporal diagram [Fig. 3(b)] using white dashed line for leading and black for trailing and sedimentary fronts.

Flow develops through three stages after releasing the gate. Within each stage, the velocity of interpenetration takes a steady value given by the balance of forces acting in the flow. During stages I and II, buoyant stress in order of $(\hat{\rho}_H - \hat{\rho}_L)\hat{g}\hat{D}$ is initially balanced by inertial stress as $(\hat{\rho}_H + \hat{\rho}_L)\hat{V}^2$, and later it is controlled by viscous stress, $(\hat{\rho}_H + \hat{\rho}_L)\hat{\nu}_{\text{av}}\hat{V}/\hat{D}^2$. Therefore, the respective characteristic velocities for *inertial* and *viscous* phases are obtained as

$$\hat{V}_t = \sqrt{\frac{1-\psi}{1+\psi}\hat{g}\hat{D}}, \tag{1}$$

$$\hat{V}_\nu = \frac{1-\psi}{1+\psi}\frac{\hat{g}\hat{D}^2}{\hat{\nu}_{\text{av}}}, \tag{2}$$

where, $\psi = \hat{\rho}_L/\hat{\rho}_H(\phi_0)$ is density ratio of the light fluid to heavy suspension, and $\hat{\nu}_{\text{av}}$ is the average kinematic viscosity of heavy and light fluids [6,7]. Saha *et al.* (2013) [28] showed an additional stage (stage III) for flow in horizontal tilt angle, during which, particle settling gradually diminishes the driving buoyancy force through reducing the effective density difference, consequently, flow reaches an abrupt *halt* over a finite distance. The behavior reported by Saha *et al.* (2013) [28] for horizontal duct ($\beta = 90^\circ$), is found to persist in the slightly inclined pipe in our experiments ($\beta = 88^\circ$). Henceforth, we use the word *sedimentary* as indication to this stage. Halt is evident in Fig. 3(a), where leading front remains almost immobile with time. There is also found a plateau corresponding to the halt distance which is evident from spatiotemporal diagram of the depth-averaged concentration in Fig. 3(b). As the flow halts, all the leading, trailing, and sedimentary fronts stop advancing [Figs. 3(a) and 3(b)]. Settling rate is often expressed as the product of Stokes slip velocity of a single particle $\hat{u}_0 = (\hat{\rho}_p - \hat{\rho}_f)\hat{g}\hat{d}^2/(18\hat{\mu}_f)$, by Richardson-Zaki hindrance function, $(1-\phi_0)^5$ [43–45]. Since the sedimentation is the only predominant process in this stage, the characteristic velocity of the sedimentary phase, $\hat{u}_s$, is defined as

$$\hat{u}_s = \frac{r_p^2(\xi-1)(1-\phi_0)^5}{18}\frac{\hat{g}\hat{D}^2}{\hat{\nu}_f}, \tag{3}$$

with $\hat{\nu}_f$ being the kinematic viscosity of the interstitial fluid. Note that ψ and ξ are convertible as $\psi = 1/(1+(\xi-1)\phi_0)$ [29]. This is typically $O(10^{-5})$ smaller than the velocities in the inertial and viscous stages, thus, the flow expectedly decelerates in the sedimentary stage. As mentioned, we consider $\hat{V}_t$ in the Eq. (1) in calculating the Reynolds number in this study. This characteristic velocity constitutes the important features of the buoyancy-driven particle-laden flows, including the density contrast between heavy and light fluids ψ as a function of ϕ_0. Regardless of the choice for the characteristic velocity, Reynolds number is always estimated to be relatively small in our experiments.

Leading front's location, $\hat{X}_f$, shown in Fig. 3(c) (inset), initially grows linearly with time, later deflects, and ultimately turns to a plateau as develops through inertial, viscous, and sedimentary phases, respectively. Inertial-viscous transition ($\hat{t} \simeq 70$ s) as well as viscous-sedimentary changeover ($\hat{t} \simeq 700$ s) are also clearly evident in this figure. Notice that the front location in Fig. 3(c) is primarily expressed in the form $\hat{X}_f^2$ to be consistent with study of Saha *et al.* [28]. The instantaneous frontal velocity $\hat{V}_f$ is determined from the local slope of the fitted curve on frontal displacement values $\hat{X}_f(\hat{t})$, thus, $\hat{V}_f = d\hat{X}_f/d\hat{t}$. As seen in Fig. 3(d), $\hat{V}_f$ gradually decreases to zero as flow comes to a halt at time $\hat{t}_s$, corresponding to the distance $\hat{X}_s$. The stoppage point is shown with an asterisk (*) in Fig. 3(c) (and its inset) corresponding to $\hat{t}_s = 978$ s and $\hat{X}_s = 213$ mm. It is clear that at this point both $\hat{X}_f$ and $\hat{X}_f^2$ reach a perfect plateau. We present $\hat{t}_s$ and $\hat{X}_s$ in Fig. 4 for various initial volume fraction of particles, ϕ_0, for a slightly angled pipe ($\beta = 88^\circ$). Both curves in Fig. 4 interestingly depict a maximum over an intermediate particle concentration ($\phi_0 = 0.30$) which is consistent with findings of Ref. [28] obtained for a strictly horizontal channel. Error bars were small,

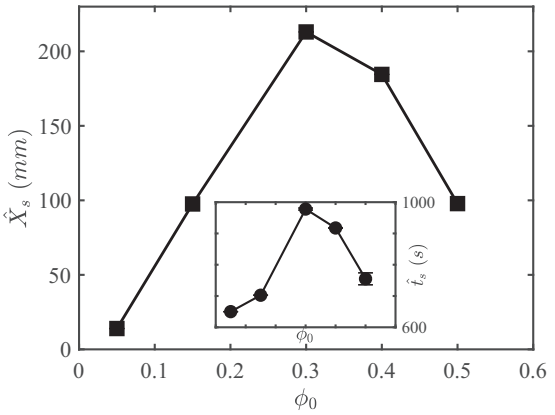

FIG. 4. Variation of the stoppage distance $\hat{X}_s$, and time $\hat{t}_s$ (inset), with initial volume fraction of particles: $\phi_0 = \{0.05,\ 0.15,\ 0.30,\ 0.40,\ 0.50\}$, $\beta = 88^\circ$, using set A, $\hat{d} = 70\ \mu$m, $\hat{\mu}_f = 0.367$ Pa s, and $\hat{u}_0 = 0.009$ mm s^{-1} ($\psi = \{0.952,\ 0.868,\ 0.767,\ 0.712,\ 0.664\}$, $\mathrm{Re}_t = \{1.37,\ 1.72,\ 1.21,\ 0.67,\ 0.22\}$, $\xi = 2.01$, and $r_p = 0.007$). Maximum $\hat{X}_s$ and time $\hat{t}_s$ correspond to the experiment with $\phi_0 = 0.30$, which is in accordance with findings of Ref. [28].

thus, not shown in this figure for clarity. This unique phenomenon can be described by looking into the competing effects of the viscosity and density of suspension. Basically, by increasing the initial volume fraction of particles ϕ_0, suspension's viscosity $\hat{\mu}_H(\phi_0) \propto (1 - \phi_0/\phi_j)^{-2}$ increases exponentially, neighboring infinity in the vicinity of packed limit ($\phi_0 \to \phi_j$). Meanwhile, the density of suspension, $\hat{\rho}_h(\phi_0) \propto \phi_0$, also increases linearly with ϕ_0. As a result, in the dilute limit viscosity is low enough to permit the spreading of suspension, yet density is also small meaning that the buoyant driving force in the exchange flow is not strong. Therefore, the heavy suspension penetrates slowly into the lighter fluid, gradually loses its momentum due to particle settling, and eventually comes to a halt at a relatively short $\hat{X}_s$. However, close to the packing limit, the driving buoyancy force of the flow is certainly increased due to the presence of solid particles. However, this increase in density is accompanied by a significant increase in viscosity which acts to decelerate the flow over a shorter stoppage distance. Over an intermediate range of ϕ_0 a common ground is achieved where density of suspension $\hat{\rho}_H(\phi_0)$ is relatively high, but the viscosity $\hat{\mu}_H(\phi_0)$ is rather moderate. That is why for such intermediate range of volume fraction ϕ_0, in Fig. 4 stoppage distance $\hat{X}_s$ is maximal compared to the dilute and packed regions. Due to the limited length (1000 mm) and experiment time (∼2000 s), only a few additional halting data points have been recorded over a range of near-horizontal angles ($75^\circ < \beta < 88^\circ$). The information is not shown in Fig. 4 for consistency. Nevertheless, the existing data is sufficient enough to see both stoppage time and distance increase with the inclination. For example, in the experiment with $\phi_0 = 0.50$, flow spreads 78% more corresponding to 60% longer time before halting when the pipe is tilted from $\beta = 88^\circ$ to 82°. Similarly, 400% more stretching and 16% longer time are reported in the experiment with $\phi_0 = 0.05$ as pipe is inclined from $\beta = 88^\circ$ to 75°.

C. Particle-laden exchange flows in inclined pipes

1. Principal characteristics

Pipe inclination transforms the behavior of flow by affecting settling and spreading processes [21]. We observed that in near-horizontal angle particles settle out perpendicular to the bottom surface of the pipe, resultantly reduce the density of suspension. Now, if the pipe is tilted away from the horizontal direction, the settling depth increases and particles stay entertained in the suspension for a longer time. Nonetheless, buoyancy force also becomes stronger with the inclination as

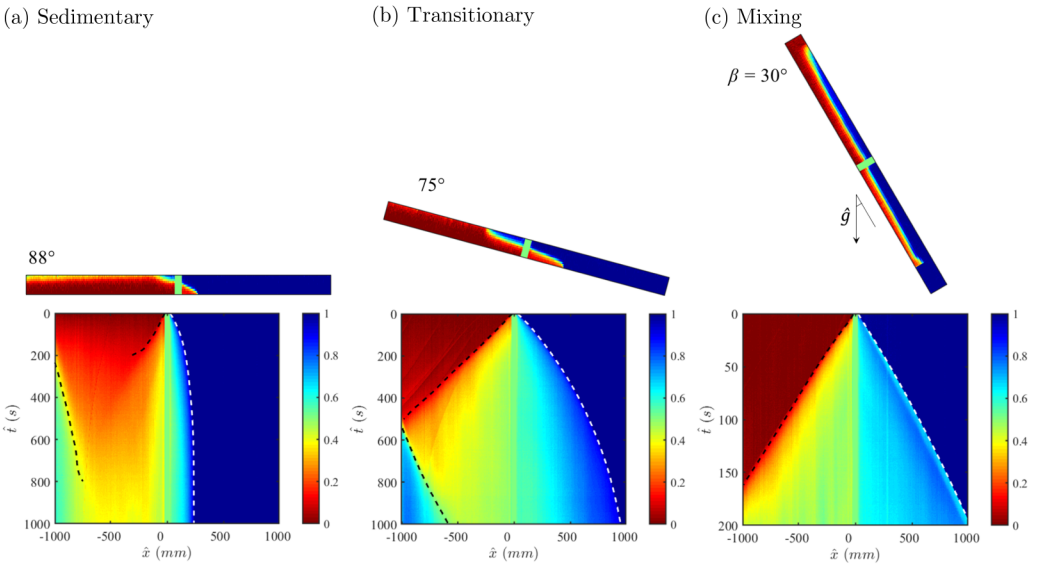

FIG. 5. Experimental images at $\hat{t} \approx 150\,\mathrm{s}$ (top) and corresponding spatiotemporal diagrams of the depth-averaged concentration (bottom) for three flow regimes (a) sedimentary, (b) transitionary, and (c) mixing: $\phi_0 = 0.30$ at $\beta = 88^\circ$, 75°, and 30°, $\hat{d} = 70\ \mu\mathrm{m}$, $\hat{\mu}_f = 0.367\,\mathrm{Pa\,s}$, and $\hat{u}_0 = 0.009\,\mathrm{mm\,s^{-1}}$ ($\psi = 0.767$, $\mathrm{Re}_t = 1.21$, $\xi = 2.01$, and $r_p = 0.007$). The field of view in snapshots is $2000 \times 9.53\,\mathrm{mm}^2$.

pipe aligns itself with the gravity orientation. The interplay between sedimentation and buoyancy-induced exchange process will decide the nature of the flow. Our experiments also confirm this interesting prediction. We observe: (i) At low particle concentrations, ϕ_0, and inclinations ($\beta \to 88^\circ$), flow is primarily controlled by sedimentation and may halt at a finite location as explained in Sec. III B. Halting occurs less frequently as the pipe is further inclined, in fact, none is observed for $\beta < 75^\circ$ over the range of particle concentrations $\phi_0 = \{0.05, 0.15, 0.30, 0.40, 0.50\}$. The advancing suspension front's position profile, $\hat{X}_f$, for such flows is curved and turns to a plateau; see Fig. 5(a). (ii) At higher ϕ_0 and inclinations ($\beta \to 0^\circ$), particles remain mixed in suspension, yet almost no significant mixing is present between two fluids. Leading and trailing fronts spread ceaselessly and linearly with time $\hat{t}$. Therefore, $\hat{X}_f$ follows a straight line [Fig. 5(c)], as one may face during viscous regime in pure-pure gravity exchange flows [6,7]. (iii) A *transitionary* domain exists between these two regimes, in which, flow manifests both *sedimentary* and *mixing* characteristics, i.e., the heavy front neither advances linearly nor comes to a halt. As a result, frontal displacement profile, $\hat{X}_f$, is curved but continues unceasingly; see Fig. 5(b). It can also be shown that the transition to mixing flows predominately occurs over angles closer to the horizon and away from the vertical direction. To distinguish the flow regimes from one another more effectively, $\hat{X}_f^2$ quantity versus time, $\hat{t}$, can be used as shown in Fig. 6. Upward-facing curves growing unboundedly with time, are related to the mixing regime. Oppositely, downward-facing curves progressing slowly to a halt are categorized under the sedimentary regime. Other types of profiles which follow neither trends, including irregular curves [Figs. 6(a)–6(c)] and straight lines [Figs. 6(d) and 6(e)], belong to the transitionary regime. With no exception, for all the values of the initial volume fraction of particles in Fig. 6(a), flow accelerates as the pipe is positioned at higher tilt angles and rapidly switches over from slow sedimentary to fast mixing flow. Since sedimentation is ineffective in the mixing regime, the viscosity is the only limiting force in the flow regulating the frontal velocity. This constraint on advancing front is manifested in displacement profiles collapsing onto a single curve at higher tilt angles; see lines with $\beta \geqslant 45^\circ$ in Figs. 6(b)–6(d). It is evident from Fig. 6 that the transitionary flows occur over a very narrow range of inclination angles. To capture these flows we had to precisely

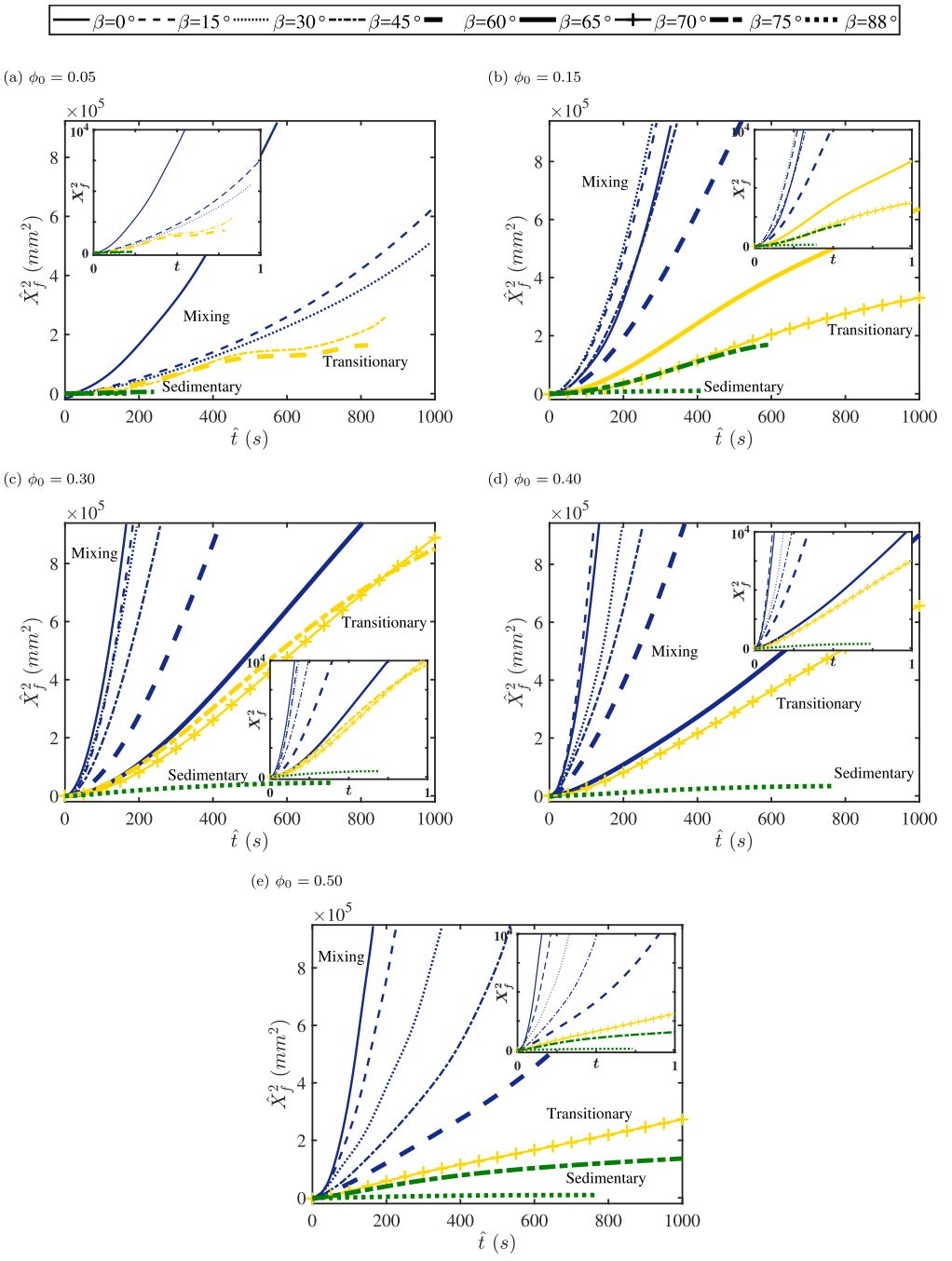

FIG. 6. Suspension front position, $\hat{X}_f^2(\hat{t})$, over time, $\hat{t}$, for various angles of inclination corresponding to the experiments in set A. Different colors correspond to sedimentary (green), transitionary (yellow), and mixing (blue) regimes: $\hat{d} = 70\ \mu$m, $\hat{\mu}_f = 0.367$ Pa s, $\hat{u}_0 = 0.009$ mm s^{-1} for (a) $\phi_0 = 0.05$, (b) $\phi_0 = 0.15$, (c) $\phi_0 = 0.30$, (d) $\phi_0 = 0.40$, and (e) $\phi_0 = 0.50$ ($\psi = \{0.952, 0.868, 0.767, 0.712, 0.664\}$, $\mathrm{Re}_t = \{1.37, 1.72, 1.21, 0.67, 0.22\}$, $\xi = 2.01$, and $r_p = 0.007$). Results in the dimensionless format are shown in the inset.

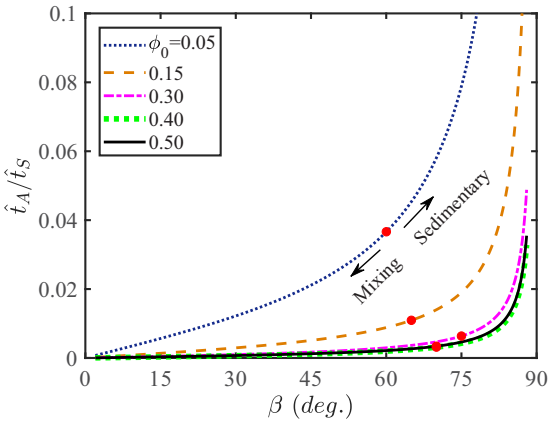

FIG. 7. The ratio of advection timescale $\hat{t}_A$, and sedimentation one $\hat{t}_S$, calculated theoretically for inclination angles $\beta \in [2^\circ,\ 88^\circ]$ in set A: $\phi_0 = \{0.05, 0.15, 0.30, 0.40, 0.50\}$, $\hat{d} = 70\ \mu$m, $\hat{\mu}_f = 0.367$ Pa s, and $\hat{u}_0 = 0.009$ mm s^{-1} ($\psi = \{0.952,\ 0.868,\ 0.767,\ 0.712,\ 0.664\}$, $\mathrm{Re}_t = \{1.37,\ 1.72,\ 1.21,\ 0.67,\ 0.22\}$, $\xi = 2.01$, and $r_p = 0.007$). The red circles are transitionary data points obtained for each line from its corresponding experiments.

design additional experiments. Although these extra tests were performed at a different time, their results are perfectly consistent with the other experiments in set A. This, on top of the benchmarking results provided in the Appendix, demonstrates the accuracy and repeatability of the experimental data presented in this study. To provide practical information for industrial design applications, we present the results in the inset of Fig. 6 and a few other figures throughout the text using the following dimensionless variables for scaling the length $\hat{x} = \hat{D}x$, velocity $\hat{V} = \hat{u}_0 V$, and time $\hat{t} = \hat{D}t/\hat{u}_0$; here, the pipe diameter $\hat{D}$ is the characteristic length, and $\hat{u}_0 = (\hat{\rho}_p - \hat{\rho}_f)\hat{g}\hat{d}^2/(18\hat{\mu}_f)$ is the Stokes settling velocity of particles.

The initial volume fraction of particles certainly impacts the flow behavior by changing the viscosity and the density of suspension. Mixing flows are likely found at higher ϕ_0 where density difference between suspension and pure fluid becomes larger. Still, the extent of influence of the particle concentration can stay limited only to mixing or sedimentary regimes. For example, all the experiments at $\beta = 30^\circ$ are mixing and ones at 88° are sedimentary in Fig. 6. The combined effects of ϕ_0 and β on the classified regimes presented in this paper can be better explained through a sedimentation-advection framework. In other words, sedimentary or mixing flow behaviors are determined by the extents that particles settle out of the flow, or are carried away along the pipe. Comparing the timescales of these processes reveals the dynamics involved in the formation of various regimes. The timescale pertaining to streamwise advection of particles by the fluid is given as $\hat{t}_A = \hat{D}/(\delta \hat{V}_v \cos\beta)$. The timescale related to the depthwise sedimentation is expressed as $\hat{t}_S = \hat{D}/(\hat{u}_s \sin\beta)$ with $\hat{D}/\sin\beta$ being approximately the depth of suspension at each angle. By increasing β, i.e., moving away from vertical, $\hat{t}_A$ increases monotonically, while $\hat{t}_S$ decreases from infinity. Figure 7 shows the ratio of these two timescales for different initial volume fraction of particles $\phi_0 = \{0.05,\ 0.15,\ 0.30,\ 0.40,\ 0.50\}$ and a full range inclination angles (except for strictly horizontal and vertical angles) in set A. The advection-to-sedimentation-timescale ratio $\hat{t}_A/\hat{t}_S$ increases as inclination decreases ($\beta \to 90^\circ$) implying that in near horizontal tilt angles, particles sediment more before being carried away by the fluid. Oppositely, the advection takes a faster pace as the pipe is tilted away ($\beta \to 0^\circ$) leaving almost no time for sedimentation. Therefore, it is expected that the sedimentation becomes more effective when the pipe is closer to the horizontal angle. For example, consider the curve at $\phi_0 = 0.15$ in the Fig. 7. At $\beta = 88^\circ$, the value of timescale ratio is almost 0.1 meaning sedimentation is 10 times slower than advection which is rather a large number for inherently slow sedimentation process compared to streamwise advection of particles

in the suspension layer. To put this into perspective, notice that the timescale ratio is calculated considering the particle concentration is uniform in the suspension ($\phi = \phi_0$). In the experiments, as the particle settling reduces the density of the suspension over time, sedimentation becomes dominant and the timescale ratio is expected to increase even more. Figure 7 also reveals that by increasing ϕ_0 the ratio $\hat{t}_A/\hat{t}_S$ decreases meaning the sedimentary behavior in the flow at a particular angle is diminished by increasing particle concentration of the mixture. This is not a surprise because sedimentation occurs slower in high-concentration suspension. It is seen that the calculated curves begin to collapse onto each other by increasing ϕ_0 leading to expectedly similar flow characteristics near the packed limit. This is evident in the experiments, for example, $\phi_0 = 0.40$ and 0.50 in set A both show transitions exactly at $\beta = 70^\circ$. We have superimposed the experimental data points where transitions occur on their associated curves in this figure. It is seen that the transition often occurs over a narrow range of β between 60° to 75°. Data points to the right of this range are mostly sedimentary and those to the left are mixing flows (shown by arrows in the figure).

Zhou *et al.* (2005) presented a similar classification for free-surface particulate film flow over a slope [21]. They reported three distinct settling behaviors: at low concentrations, ϕ_0, and inclinations (large β), particles settle out of the flow and aggregate at the bottom. At intermediate ϕ_0 and β, the suspension remains well mixed. And at higher ϕ_0 and inclinations (smaller β), particles are transported faster than fluid, accumulating in a thick ridge in the vicinity of the advancing contact line. Similar behaviors of the first and second regimes in Zhou *et al.* (2005) are also observed in downstream pipe section in our experiments corresponding to "sedimentary" and "mixing" regimes. Nevertheless, our results show no particle enrichment near the tip of the front; see Fig. 8 for images over the full range of parameters. Accumulation may occur as a result of relative transportation rate of solid and fluid [21,22]. Zhou *et al.* (2005) [21] expressed that the solid-to-fluid relative velocity is proportional to the particle settling rate $\hat{u}_s$, which in our experiments is estimated as typically $O(10^{-5})$ weaker than the characteristic velocity $\hat{V}_v$. Therefore, particles remain rather immobile with respect to the fluid in the streamwise direction. Still, in the depthwise direction, volume fraction may increase with depth by settling or decrease by the particle flux due to the gradients in concentration and shear stress [46–48]. Mirzaeian and Alba (2018) [29] showed that in narrow vertical channels, shear-induced migration effect may be neglected in front of settling one if the ratio of their fluxes (in m s^{-1}),

$$\frac{\hat{J}_{\text{Migration}}}{\hat{J}_{\text{Settling}}} = \frac{9K_v(1-\phi_0/\phi_j)^2}{\psi(\xi-1)}\frac{1-\psi}{1+\psi}, \tag{4}$$

is infinitesimal. Constant $K_v \approx 0.62$ corresponds to shear-induced particle flux due to a gradient in effective viscosity of the suspension [47]. The ratio in Eq. (4) is approximately 0.05–0.25 for our range of study, implying that the migration effects may not be too small in presented experiments (up to 25% of settling flux). As a visual example, consider the experiment at $\beta = 60^\circ$ in Fig. 8(b). For this experiment at $\hat{t} \approx 248$ s with $\hat{u}_s = 0.004\,\text{mm s}^{-1}$, a sediment layer with 1-mm thickness is expected (pipe width is approximately 10 mm). However, the concentration across the thickness of the leading front seems to be uniform in this figure. One may relate the reduced particle settling to the migration flux due to the high shear rate at this angle. In regard to the Brownian motion of particles, Espin and Kumar (2014) [38] showed if $\delta^2\text{Pe} \gg 1$ meaning the particle size being $\hat{d} \gg 1\,\mu$m, particle self-diffusion across the suspension is insignificant which is also the case in our experiment. To demonstrate this, we evaluate the Peclet number $\text{Pe} = \hat{V}_t\hat{D}/\hat{D}_0$ for the suspension in our experiments. $\hat{D}_0$ is the Einstein diffusivity, defined by $\hat{D}_0 = k_B\hat{T}/(3\pi\mu_f\hat{d})$ where k_B is the Boltzmann constant, $\hat{T}$ is the characteristic temperature, and $\hat{d}$ is particle diameter [38]. $\hat{D}_0$ for set A is estimated to be of the order of $O(10^{-17})\,\text{m}^2\,\text{s}^{-1}$ corresponding to $\text{Pe} \sim O(10^{13})$ and $\delta^2\text{Pe} \sim O(10^9)$, indicating the particle self-diffusion is negligible. Therefore, settling and shear-induced migration fluxes are the only major diffusive processes across the pipe; also see Refs. [49,50] for the self-diffusion of binary fluid (glycerol-water solution) in presence of the solid particles.

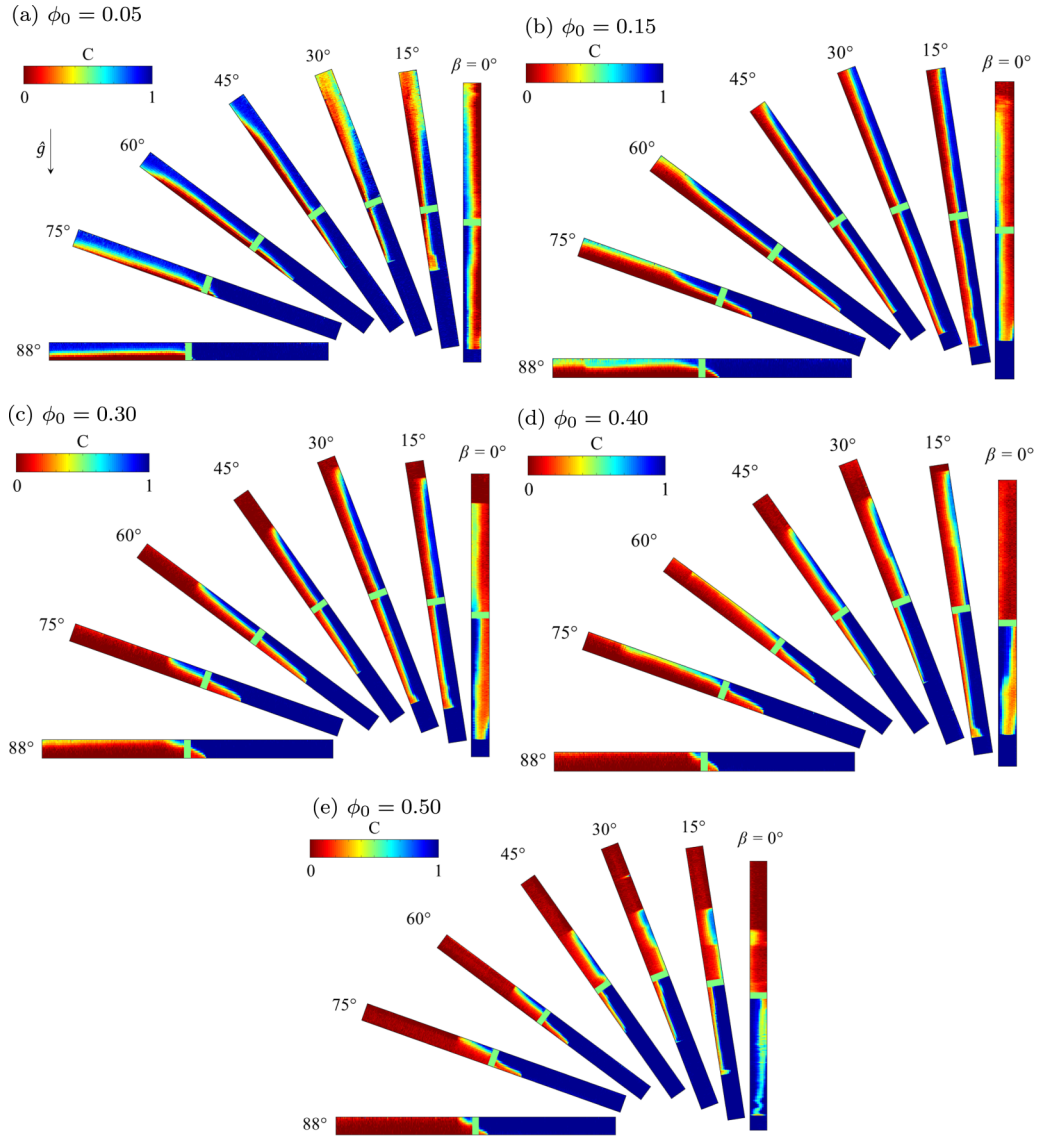

FIG. 8. Array of experimental images at various angles for same experiments as in Fig. 6 recorded at: (a) $\hat{t} = 484 \pm 32$ s, (b) $\hat{t} = 248 \pm 12$ s, (c) $\hat{t} = 141 \pm 13$ s, (d) $\hat{t} = 101 \pm 9$ s, and (e) $\hat{t} = 153 \pm 35$ s. The field of view is 2000×9.53 mm^2.

Let us now focus on the irregular protuberance observed at the forefront of some experiments, for example, the one at $\beta = 15^\circ$ with $\phi_0 = 0.30$ in Fig. 8(c). For a closer look, consider Fig 9 showcasing this experiment. The mean concentration, $\bar{C}$, in the right-hand pipe is presented for a sequence of recordings in this figure. It is clear that the spike in concentration at the advancing front is caused by a bump at the tip of the leading front. Similar patterns are often observed in our experiments with intermediate volume fraction ϕ_0, and in pipes tilted away from horizontal ($\beta \to 0^\circ$); see for example $\beta = 15^\circ$ and 30° in Figs. 8(b)–8(d). In the absence of particle enrichment, the bump is solely caused by three-dimensional inertial effects. The spreading front usually evolves in the form of the "inertial bump" when its height adapts according to the Bernoulli pressure difference as a result of the velocity variation between the tip of the front and the fully-developed

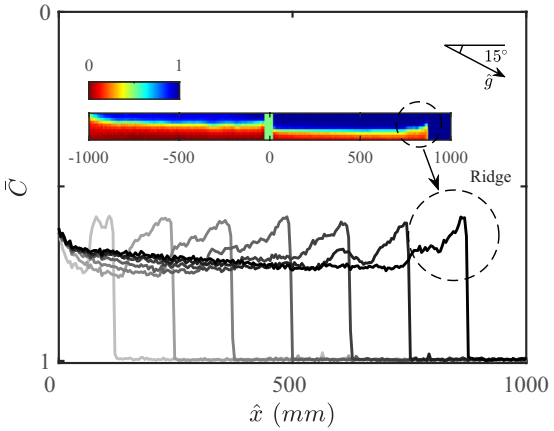

FIG. 9. Concentration profiles on the right-hand side of the pipe at times $\hat{t} = [0, 23, 46 \ldots 138, 161]$ s, showing the formation of a ridge close to the front region. $\phi_0 = 0.30$, $\beta = 15^\circ$, $\hat{\mu}_f = 0.367$ Pa s, and $\hat{u}_0 = 0.009$ mm s^{-1} ($\psi = 0.767$, $\mathrm{Re}_t = 1.21$, $\xi = 2.01$, and $r_p = 0.007$).

laminar flow behind it [7,51]. The height and the stretch length of these bumps may vary with ϕ_0 and β; see Fig. 8. Further detailed analysis of ridge formation at the front is beyond the scope of this paper. It should be pointed out that in the same figure for the vertical cases, suspension seems to move downward in the vicinity of the right wall instead of in a perfectly axisymmetric downfall. Nonetheless, it is not extremely unusual for an exchange flow of two miscible fluids in a vertical geometry to exhibit an asymmetric interface. In fact, Kerswell [52] theoretically showed there is a chance for the coaxial exchanging fluids to reveal certain slumping side-by-side or concentric/eccentric core-annular patterns in the pipe. Without doubt, experimental conditions can redistribute the probability of each pattern. In our experiments, the design and operation of the gate valve can be the major factor for this phenomenon. We used a double-acting pneumatic-solenoid gate valve (from VAT Valves) that operates quickly and smoothly. At lower inclinations, the shape of the interface is not influenced by the way the gate opens. At the vertical angle, however, the gate is biased toward a side-by-side pattern rather than a core-annular one as it opens sliding side-to-side. Regardless, these effects are only limited to the initial stage after the gate release and have no considerable impact on the long-time behavior of the flow. Our benchmarking results against Seon *et al.* (2005) [6] shown in Fig. 15 for front velocity and macroscopic diffusion coefficient of pure fluids further verify this.

We have summarized flow classification results for set A in the phase diagram of Fig. 10(a). Mixing cases shown by (■) belong to a domain as specified by intermediate particle concentration and high inclination (see area below the dashed line). We expect to find fewer mixing flows in dilute limit ($\phi_0 \to 0$) and none at $\phi_0 = 0$, where there is no driving density difference to set off the exchange flow. The same trend is presumed for the packed limit ($\phi_0 \to \phi_j$) where effective viscosity $\hat{\mu}_H(\phi_0) = \hat{\mu}_f(1 - \phi_0/\phi_j)^{-2}$ becomes extremely high so that suspension will be overly packed and almost immobilized. This explains the predicted deflection of mixing domain's bound over higher volume fraction, ϕ_0, in Fig. 10(a). Furthermore, due to the strong sedimentation in the limit of nearly horizontal pipes ($\beta \to 90^\circ$), all experiments in this region are classified as sedimentary and shown by (●) in the phase diagram. A few sparse transitionary data points adjacent to the mixing domain are also shown in this figure as (▲) that make up for approximately 20% of all cases. The experiments with a ridge at the leading front are also marked in Fig. 10(a), including a domain with medium ϕ_0 and small β. The implication is that at least some forms of inertial bump appear in the majority of mixing experiments.

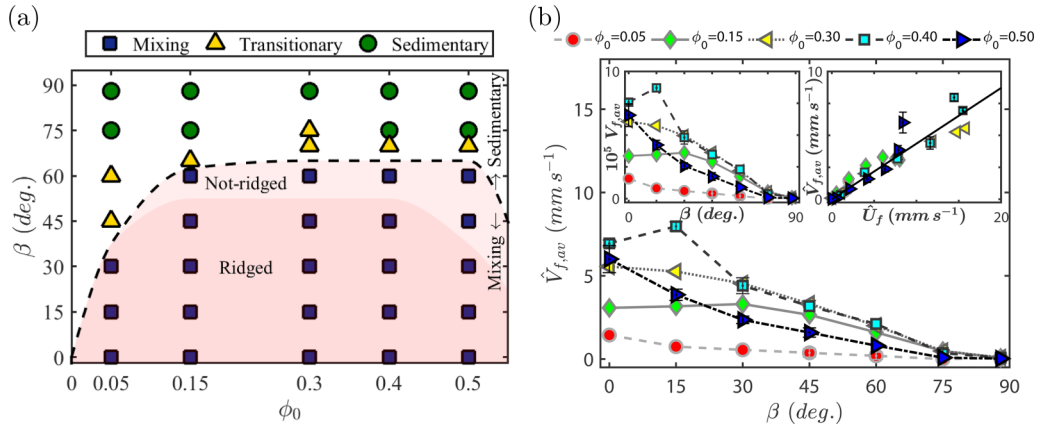

FIG. 10. (a) Phase diagram, and (b) variation of the mean frontal velocity $\hat{V}_{f,\mathrm{av}}$, versus angle of inclination β, for experiments in set A: $\phi_0 = \{0.05, 0.15, 0.30, 0.40, 0.50\}$, $\hat{d} = 70\ \mu$m, $\hat{\mu}_f = 0.367$ Pa s, and $\hat{u}_0 = 0.009$ mm s^{-1} ($\psi = \{0.952, 0.868, 0.767, 0.712, 0.664\}$, $\mathrm{Re}_t = \{1.37, 1.72, 1.21, 0.67, 0.22\}$, $\xi = 2.01$, and $r_p = 0.007$). Right inset (subfigure b): $\hat{V}_{f,\mathrm{av}}$ plotted against the velocity scale $\hat{U}_f$ for experiments in set A; the fitted line is given by Eq. (6) with the slope $C_F = 0.435$. Left inset: dimensionless mean frontal velocity $V_{f,\mathrm{av}}$ with β.

An important characteristic which is of interest to geophysical and industrial processes is how fast the heavy suspension layer advances within duct upon its release into a light ambient. We have obtained the mean frontal velocity, $\hat{V}_{f,\mathrm{av}}$, by averaging $\hat{V}_f$ at long times when the flow proceeds steadily (variation in velocity is less than 10%). Figure 10(b) presents measured mean frontal velocities for all the experiments in set A. $\hat{V}_{f,\mathrm{av}}$ grows expectedly with the inclination (or decrease in β) since the driving buoyancy force in streamwise direction increases (depthwise sedimentation also decreasing). Furthermore, higher velocities are interestingly found over an intermediate range of particles volume fraction, away from dilute ($\phi_0 = 0.05$) and dense limits ($\phi_0 = 0.50$). This phenomenon can be explained by considering the intricate effect of ϕ_0 on heavy fluid's density and viscosity. The ratio of the density of light to heavy fluid, $\psi = \hat{\rho}_L/\hat{\rho}_H(\phi_0)$, decreases with ϕ_0, ultimately resulting in a larger driving buoyancy force (increasing $\hat{V}_{f,\mathrm{av}}$). In the vicinity of packing concentration, however, effective viscosity $\hat{\mu}_H(\phi_0)$, grows exceedingly [$\hat{\mu}_H(\phi_0) \propto (1 - \phi_0/\phi_j)^{-2}$]; viscous dissipation is strong and flow motion is highly restrained (decreasing $\hat{V}_{f,\mathrm{av}}$). That is why a maximal interpenetration rate, $\hat{V}_{f,\mathrm{av}}$, is achieved over an intermediate volume fraction.

Let us now investigate whether the dimensional front speeds in Fig. 10(b) can be predicted (scaled) using an appropriate velocity scale. Herbolzheimer and Acrivos (1981) suggested that for batch sedimentation in an inclined channel (Boycott flow), the motion of the descending suspension-clear-fluid interface to be enhanced according to $\Lambda^{1/3}\cos^2\beta$ [18]. Here, $\Lambda = 18\phi_0/[(1-\phi_0)^5 r_p^2]$ is the ratio of the sedimentation Grashof number to the Reynolds number Re_t, representing the combined effects of the pipe geometry and the kinematics of sedimentation. In our case, since we face an exchange flow between the heavy and light phases, governed by viscous-buoyant stress balance [Eq. (2)], $\Lambda^{1/3}\cos^2\beta$ enhancement term may be multiplied by $\hat{V}_v$. In other words, a velocity scale, $\hat{U}_f$, may be constructed as

$$\hat{U}_f = \hat{V}_v \Lambda^{1/3}\cos^2\beta. \tag{5}$$

The right inset in Fig. 10(b) does, in fact, reveal the effectiveness of such scaling. Except for the vertical pipe [high $\hat{U}_f$ values in Fig. 10(a)], velocities collapse agreeably on a line given as

$$\hat{V}_f = C_F \hat{U}_f, \tag{6}$$

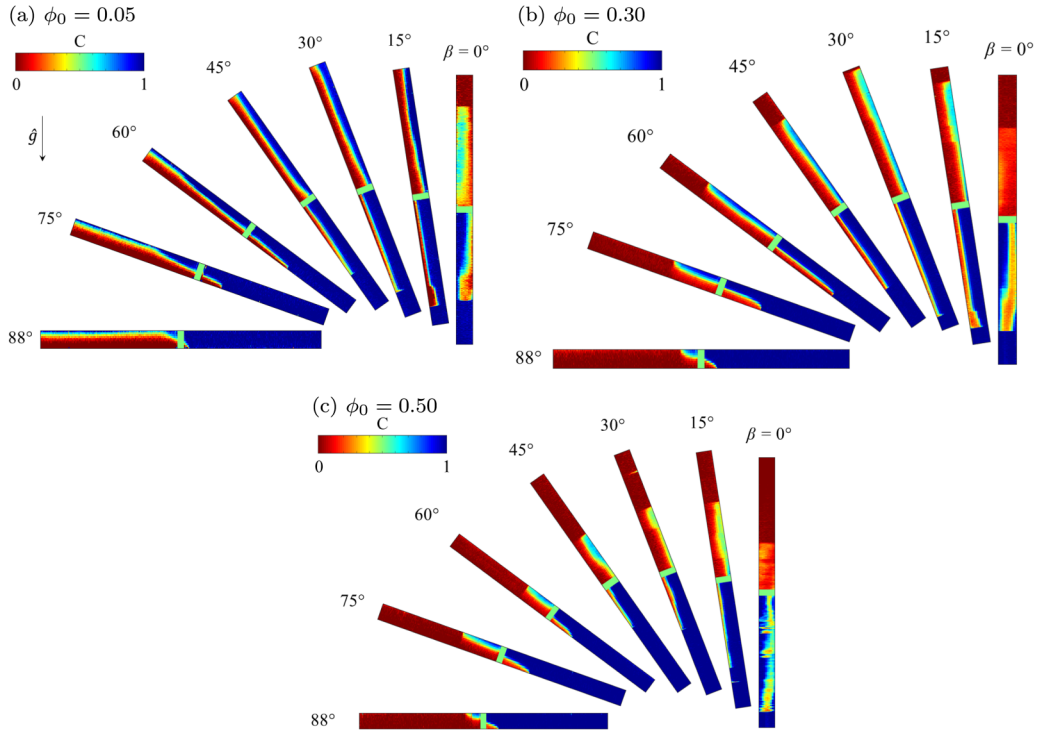

FIG. 11. Array of experimental images at various angles corresponding to the experiments of set B: $\hat{d} = 40\ \mu$m, $\hat{\mu}_f = 0.367$ Pa s, $\hat{u}_0 = 0.003$ mm s^{-1} for (a) $\phi_0 = 0.05$ at $\hat{t} = 778 \pm 51$ s, (b) $\phi_0 = 0.30$ at $\hat{t} = 200 \pm 26$ s, and (c) $\phi_0 = 0.50$ at $\hat{t} = 165 \pm 59$ s ($\psi = \{0.952,\ 0.767,\ 0.664\}$, $\mathrm{Re}_t = \{1.37,\ 1.21,\ 0.22\}$, $\xi = 2.01$, and $r_p = 0.004$). The field of view is 2000×9.53 mm^2.

with $C_F = 0.435$ being the slope of the fitted curve (line). In fact, $\hat{U}_f$ can be $\sim O(10^2)$ greater than the characteristic velocity of the pure viscous flow, $\hat{V}_\nu$. Therefore, we can substantiate that Boycott-type enhanced flow rate in the clarified layer which is exclusively revealed in suspension exchange flows in inclined pipes, indeed facilitates the evolution of fronts. Nonetheless, the same statement is simply invalid for the vertical pipe where such an effect is nonexistent. Now that the front velocity is revealed to be substantially larger than the viscous characteristic velocity $\hat{V}_\nu$, it is important to investigate whether flow remains viscous in all the experiments. For this purpose, we define a new Reynolds number, $\mathrm{Re}_f = \hat{\rho}_H(\phi_0)\hat{U}_f\hat{D}/\hat{\mu}_H(\phi_0)$, where $\hat{\rho}_H(\phi_0)$ and $\hat{\mu}_H(\phi_0)$ are the density and the viscosity of the suspension, respectively. The range of the Reynolds number in set A is $\mathrm{Re}_f \in [0.46,\ 172]$ with larger values are obtained for the intermediate ϕ_0. This is expectedly up to a hundred times larger than the Reynolds number defined earlier in this paper ($\mathrm{Re}_t \in [0.22,\ 1.72]$). According to Seon *et al.* (2007) [7], as long as the heavy and light layers stretch segregated with no intermixing or interfacial instability (that is the case in our experiments), we consider the flow viscous; see Fig. 8. In fact, the physical factor preventing the inertial instability and mixing between suspension and pure layers is the extremely high viscosity of suspension which can be up to $O(10^4)$ greater than that one of water. Nevertheless, inertial forces are still found to be active in the flow to some extent, causing inertial bumps at the tip of the suspension layer at higher inclinations. We have further analyzed the variation of the mean frontal velocity $\hat{V}_{f,\mathrm{av}}$ with the Reynolds number Re_f in the experiments, however, the results are not presented here for brevity. At first, it seems $\hat{V}_{f,\mathrm{av}}$ generally increases with ϕ_0 in a way that the measured velocities are arranged in separate clusters corresponding to their values of the initial volume fraction of particles. Secondly, it appears that the mean frontal velocities in experiments with a common ϕ_0 increase linearly with Re_f except the one

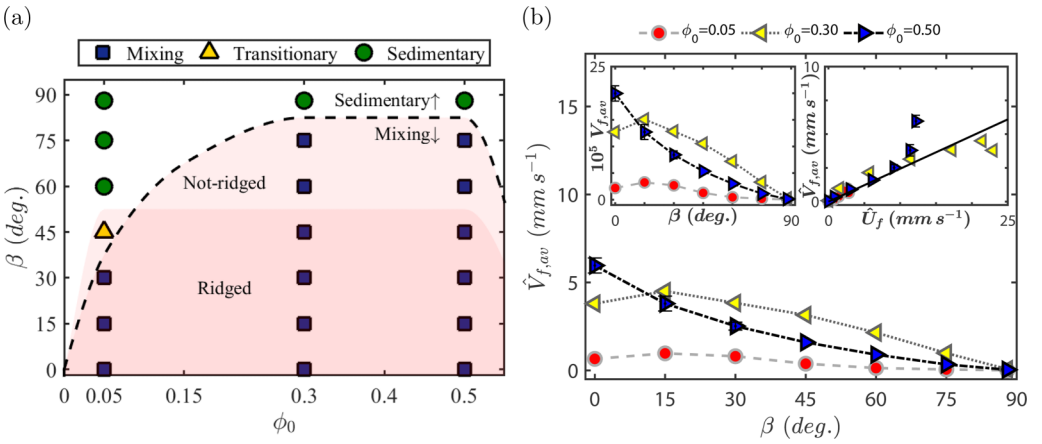

FIG. 12. (a) Phase diagram and (b) variation of the mean frontal velocity $\hat{V}_{f,\mathrm{av}}$, versus angle of inclination β, for experiments in set B: $\phi_0 = \{0.05, 0.30, 0.50\}$, $\hat{d} = 40$ μm, $\hat{\mu}_f = 0.367$ Pa s, and $\hat{u}_0 = 0.003$ mm s^{-1} ($\psi = \{0.952,\ 0.767,\ 0.664\}$, $\mathrm{Re}_t = \{1.37,\ 1.21,\ 0.22\}$, $\xi = 2.01$, and $r_p = 0.004$). The fitted line in the right inset is given by Eq. (6) with the slope $C_F = 0.244$.

at the strictly vertical angle. On this basis, it is clear that the interpenetration velocity at a specific angle β is directly characterized by the initial volume fraction of particles in the suspension ϕ_0 and the Reynolds number of the flow Re_f.

2. Effect of particle size

For a comprehensive and independent evaluation of each flow parameter in particle-laden exchange current, the density mismatch of heavy and light phases, $\psi = 1/[1 + (\xi - 1)\phi_0]$, is preserved throughout all three experimental sets ($\xi = \hat{\rho}_p/\hat{\rho}_f \approx 2$). The settling velocity, $\hat{u}_0$, is then reduced via two ways: (1) Using smaller particles, the results of which are presented in this section. (2) Choosing a more viscous fluid (to be presented in Sec. III C 3). We have carried out a total of 21 experiments using smaller particles of the same density, shape, and distribution within the same fluid; see set B in Table III. Range of initial particle concentration is $\phi_0 = \{0.05,\ 0.30,\ 0.50\}$, and experiments cover full range of inclination angles ($\beta \in [0^\circ, 88^\circ]$). Herein, only parameters involving particle size $\hat{d}$, such as particle-to-pipe-diameter ratio r_p, and the settling velocity $\hat{u}_s \propto r_p^2$ are reduced; see Eq. (3). All other parameters in Tables I and II remain unchanged; see snapshots of set B experiments given in Fig. 11. We use a similar method as explained previously to classify the flow and present the results in Fig. 12(a). Interestingly, the boundary of the mixing regime is slightly shifted upward, meaning that the transition from sedimentary to mixing flows occurs even at closer angles to the horizontal direction. This behavior is well expected since the buoyant stress, scaled as $(1 - \psi)\hat{g}\hat{D}$, is unaffected by the change of particle size $\hat{d}$, meanwhile reduced sedimentation permits particles stay mixed in the flow for a longer time. The advection-to-sedimentation-timescale ratio $\hat{t}_A/\hat{t}_S$ presented earlier for set A (Fig. 7), is found to decrease as smaller particles are used, also suggesting that the sedimentary effect has to be weakened in set B. It is also very interesting that the periphery of the ridged domain in the phase diagram remains rather untouched regardless of the particle size; compare Fig. 12(a) with Fig. 10(a). This reiterates the fact that in the absence of significant relative velocity between solid and fluid phases along the pipe, bumps originate from the inertial effects at the tip and are certainly independent of settling behavior of particles. Through visual examples of the experiments in Fig. 11, it can be also observed that the particle-enrichment is insubstantial along the leading front; for example, see the image at $\beta = 75^\circ$ with $\phi_0 = 0.30$ in this figure.

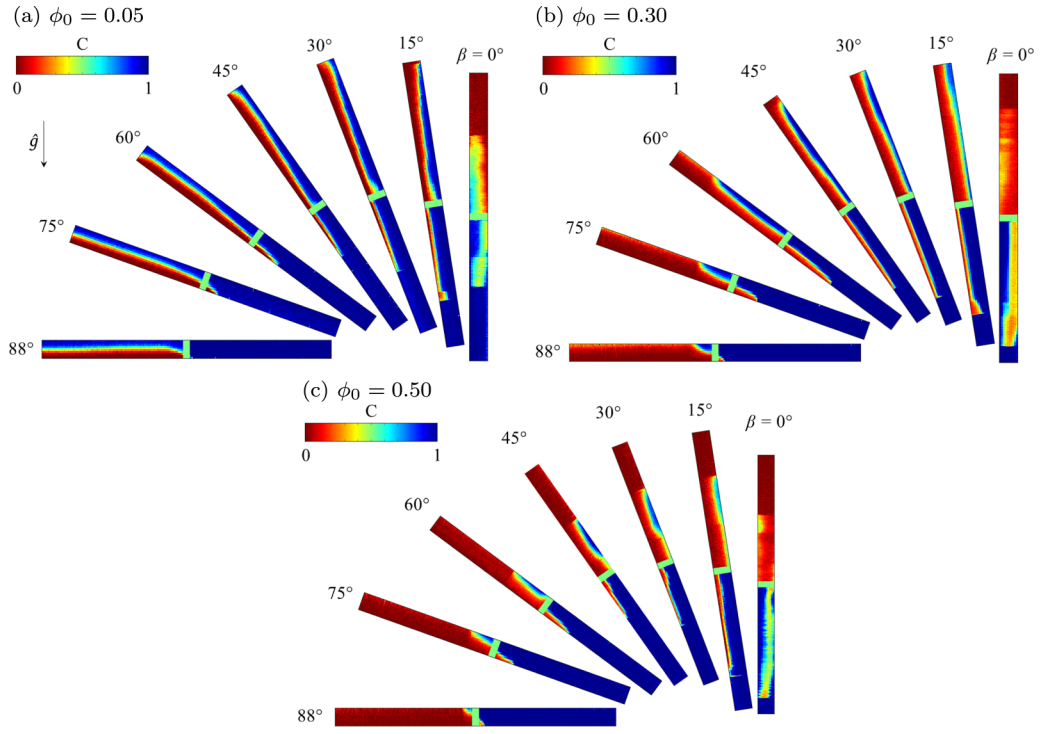

FIG. 13. Array of experimental images at various angles corresponding to the experiments of set C: $\hat{d} = 70\ \mu$m, $\hat{\mu}_f = 0.765$ Pa s, $\hat{u}_0 = 0.004$ mm s^{-1} for (a) $\phi_0 = 0.05$ at $\hat{t} = 882 \pm 52$ s, (b) $\phi_0 = 0.30$ at $\hat{t} = 323 \pm 42$ s, and (c) $\phi_0 = 0.50$ at $\hat{t} = 251 \pm 18$ s ($\psi = \{0.953,\ 0.770,\ 0.668\}$, $\mathrm{Re}_t = \{0.66,\ 0.58,\ 0.10\}$, $\xi = 1.99$, and $r_p = 0.007$). The field of view is 2000×9.53 mm^2.

Apart from the vertical pipe ($\beta = 0°$), the trends in $\hat{V}_{f,\mathrm{av}}$ for experiments with smaller particles (set B) in Fig. 12(b), seem to be consistent with those of larger particles [set A shown previously in Fig. 10(b)]. Front velocity consistently decreases with β and is maximal over a range of intermediate ϕ_0. The decrease in particles' settling rate does not have a sizable impact on the advancement of front; compare $\hat{V}_{f,\mathrm{av}}$ values between Figs. 10(b) and 12(b). The scaled results presented in the right inset of Fig. 12(b), display a collapse on a line with the equation in form of Eq. (6) with the constant $C_F = 0.244$. Note that C_F has decreased equiproportional with r_p in experiments of set B with respect to set A, implying that $C_F = f(r_p)$.

3. Effect of fluid's viscosity

The fluid's viscosity $\hat{\mu}_f$ affects the flow behavior remarkably by controlling: (1) settling rate $\hat{u}_s \propto 1/\hat{\mu}_f$ [see Eq. (3)], and simultaneously (2) the spreading rate through adjusting the effective viscosity of suspension $\hat{\mu}_H(\phi_0) = \hat{\mu}_f(1 - \phi_0/\phi_j)^{-2}$. We have designed 21 additional experiments by suspending the same particles of set A, this time, in a fluid almost twice as viscous with nearly the same density (variation was <1%; see set C in Table III). As a consequence, $\hat{\mu}_H$ is increased, thus, lowering $\hat{u}_s$ and Re_t, while all other parameters remain unchanged. See Fig. 13 for the experimental images belonging to set C. Counterintuitively, extents of domains in the phase diagram given in Fig. 14(a) are in an identical fashion of those in set A shown in Fig. 10(a). It is valid to conclude that the fluid's viscosity consistently influences the settling and spreading processes to the same extents, thus, the regime transition is immaterial of $\hat{\mu}_f$. In other words, even though the settling speed of particles is decreased as $\hat{\mu}_f$ increases, the exchange flow also develops more slowly, which

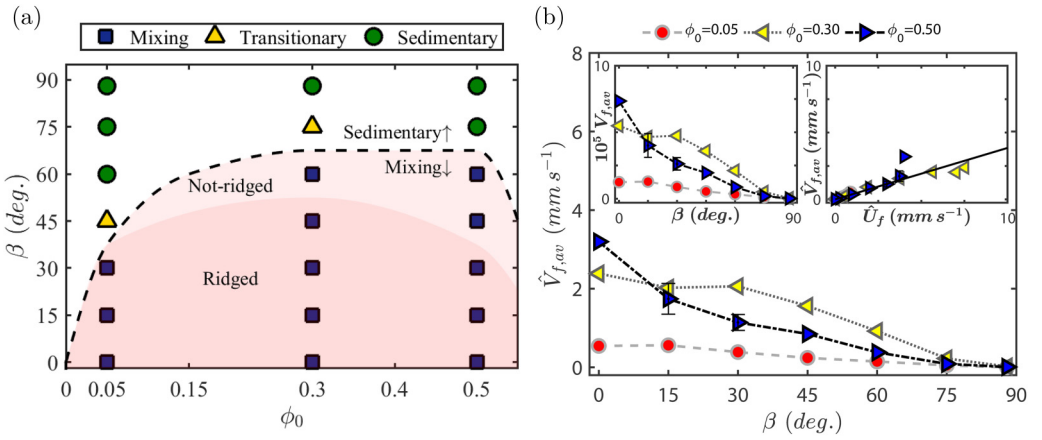

FIG. 14. (a) Phase diagram and (b) variation of the mean frontal velocity $\hat{V}_{f,\mathrm{av}}$, versus angle of inclination β, for experiments in set C: $\phi_0 = \{0.05, 0.30, 0.50\}$, $\hat{d} = 70$ μm, $\hat{\mu}_f = 0.765$ Pa s, and $\hat{u}_0 = 0.004$ mm s^{-1} ($\psi = \{0.953,\ 0.770,\ 0.668\}$, $\mathrm{Re}_t = \{0.66,\ 0.58,\ 0.10\}$, $\xi = 1.99$, and $r_p = 0.007$). The fitted line in the right inset is given by Eq. (6) with the slope $C_F = 0.385$.

in turn provides enough time for sedimentation. Of course, the timescale $\hat{t}_A/\hat{t}_S$ remains perfectly unchanged here compared to the set A. By increasing the viscosity of the fluid, $\hat{V}_{f,\mathrm{av}}$ decreases in all experiments with regard to set A; compare the results in Fig. 14(b) to Fig. 10(b). Note that by increasing $\hat{\mu}_f$ both the viscosities of suspension and pure phases are increased leading to overall flow slowdown (decrease in $\hat{V}_{f,\mathrm{av}}$). Again, here the scaled velocities collapse onto a line similar to Eq. (6) with the slope $C_F = 0.385$. This constant also varies adversely with the viscosity, suggesting that in general $C_F = f(r_p, \hat{\mu}_f)$. Therefore, it is advised that C_F values given in this manuscript are valid only over a certain range of flow parameters and should not be generalized to different circumstances (see Tables I and II).

IV. CONCLUSIONS

Suspension gravity current in a narrow lock-exchange pipe has been studied experimentally over a range of initial particle concentrations, ϕ_0, at low Reynolds numbers. Due to the small density difference and high viscosity, the heavy-light interface remains mostly unperturbed and with insignificant mixing across the pipe. As a result, the interface is stretched between counter parallel layers of suspension moving downstream, and light pure fluid advancing upstream. For pipes even slightly inclined, a novel interface is formed behind the suspension (sedimentary front). The interpenetration rate of the heavy and light layers is limited by the trade-off between the depthwise settling as well as streamwise spreading. By inclining the pipe from nearly horizontal to vertical angles, three distinct regimes have been observed: (1) sedimentary: in the near-horizontal pipes, buoyancy force is first balanced by inertia, later by viscosity, and at long times is controlled by sedimentation. The spreading velocity decreases constantly to zero until flow halts at a finite distance. The halt time and distance are found to be maximal over an intermediate range of particles volume fraction. (2) Mixing: away from nearly horizontal angles, the depthwise settling negligibly affects the spreading of fronts. Particles stay mixed in the suspension and flow advances through a viscous-buoyancy equilibrium. The front velocity then reaches a constant non-zero value. While the streamwise motion of particles relative to the fluid is negligible, their migration opposite to the depthwise direction has proved to help to keep them suspended within the carrying fluid. (3) Transition between sedimentary and mixing regimes occurs abruptly at angles closer to horizontal. Flow in this regime partly demonstrates the sedimentary and mixing behaviors.

Classification of the sedimentary, mixing, and transitionary flows are proposed in the dimensionless map of β and ϕ_0, suitable for industrial design and planning applications. Protuberances in the form of inertial bumps frequently have appeared in mixing regime. Front velocity is shown to be generally higher for the flows corresponding to the mixing domain. Using a scaling factor which simultaneously constitutes the viscous-buoyant as well as Boycott features of the flow allows us to accurately predict the frontal velocity variation—at least away from strictly vertical angles—as given in Eq. (6). Preserving the density contrast between heavy and light fluids, the effects of reducing particle size and increasing fluid's viscosity have further been investigated. Essentially, both reduce the settling rate of particles, with the only difference being that by increasing the fluid's viscosity, current is further restrained. Therefore, the sedimentary behavior is diminished in the former while it remains approximately the same in the latter. Consequently, flow undergoes a phase transition at lower inclination if smaller particles are used, whereas transitions occur invariably over the same range of angles regardless of the fluid's viscosity. The last note here is that additional experiments need to be carefully designed to compare against our recent theoretical study [29]. As well as matching fluids and particle densities, a special gate valve needs to be considered to mimic the flow configuration assumed in the lubrication model, namely, suspension wetting the wall and pure fluid moving through the core.

As an extension to this work, exploring the practical effects of bidensity (polydensity) particles in suspension would be of interest, which has been experimentally investigated for debris flow by Lee *et al.* (2014) [53]. Moreover, the displacement flow of suspension by pumping a Newtonian pure fluid or vice versa, similar to the work of Alba *et al.* (2013) [8], appears to be a valid continuation to our experiments, with potential industrial significance in the context of slurry removal as well as hydraulic fracturing processes. It is anticipated that imposing a mean flow on the lock-exchange configuration can strongly influence the dynamics of the particle-laden flow, and may even reveal rather more intrinsic effects. In this case, sedimentary or mixing flow behaviors in the pipe can be determined by a trade-off between the rate of particle settling and the superimposed flow velocity.

ACKNOWLEDGMENTS

This research has been carried out at the University of Houston (UH) using the startup funds of K.A. We thank Hector Garza for his assistance during designing and realizing the experimental set-up.

APPENDIX: BENCHMARKING AGAINST PURE (PARTICLE-FREE) EXCHANGE FLOW STUDY OF SEON *et al.* (2005) [6]

We have used solution of water and NaCl salt for the heavy fluid, and fresh water dyed with non-waterproof black ink (1600 mg/l) for the light one. The density difference between heavy and light fluids is characterized by Atwood number as $\mathrm{At} = (\hat{\rho}_H - \hat{\rho}_L)/(\hat{\rho}_H + \hat{\rho}_L) = (1-\psi)/(1+\psi)$ and interpenetrating rate by Reynolds number, $\mathrm{Re}_t = \hat{V}_t \hat{D}/\hat{\nu}_f$. We performed 33 experiments covering $\beta \in [0^\circ, 88^\circ]$ and $\mathrm{At} = 0.0035$, 0.01 and 0.04 ($\mathrm{Re}_t \in [170, 600]$). Validity of these experiments are ensured via four ways: (1) Seon *et al.* (2005) [6] classified various viscous, transitionary, and mixing regimes using the dimensionless controlling parameter $\mathrm{Re}_t \cos\beta$. This quantity represents the relative strength of streamwise buoyant $\Delta\hat{\rho}\hat{g}\hat{D}\cos\beta$ to viscous stresses $\hat{\mu}\hat{V}_t/\hat{D}$ [8]. Seon *et al.* (2005) [6] found that the changeover from viscous to transitionary flows happens at $\mathrm{Re}_t \cos\beta \approx 50$. Our experimental results presented in Fig. 15(a) also confirm such transition. (2) The frontal velocity variation with inclination in the viscous domain is reported as $\hat{V}_f/\hat{V}_t = [(1/16 - 1/(2\pi^2)]\mathrm{Re}_t \cos\beta$ [6] which is in close agreement to our prediction shown as inclined dashed line in Fig. 15(a). (3) Furthermore, frontal velocities in the transitionary domain collapse onto a plateau with maximum value $\hat{V}_f/\hat{V}_t \approx 0.7$ as shown by horizontal dashed line remaining almost independent of inclination. (4) The heavy and light interpenetrating velocities in the diffusive flow domain are relatively low due to the effective transverse mixing [6]. For such flows, it is valid to assume a rather

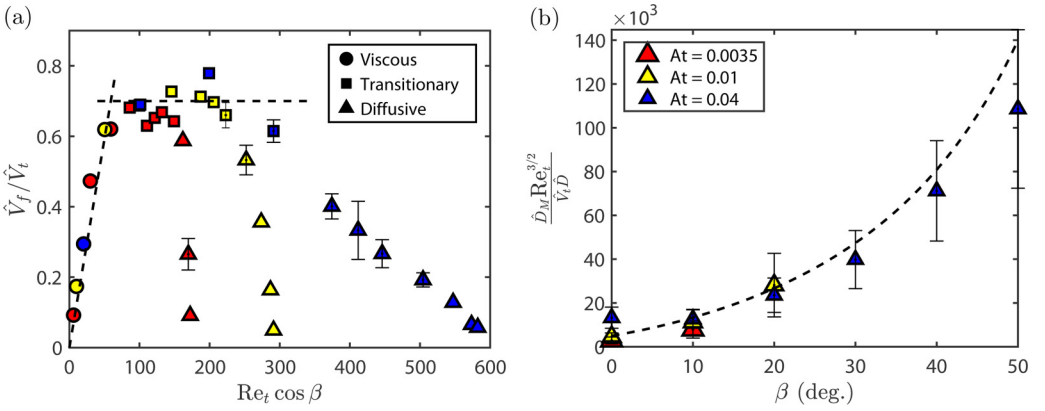

FIG. 15. Benchmarking result of pure exchange limit against Ref. [6]: (a) dependency of $\hat{V}_f/\hat{V}_t$ on $\mathrm{Re}_t \cos\beta$ for viscous (●), transitionary (■), and diffusive (▲) regimes showing complete agreement with the findings of Ref. [6]. Different colors correspond to At = 0.0035 (red), At = 0.01 (yellow), and At = 0.04 (blue); the oblique dashed line corresponds to $\hat{V}_f/\hat{V}_t = [(1/16 - 1/(2\pi^2)]\mathrm{Re}_t \cos\beta$ and the horizontal dashed line corresponds to $\hat{V}_f/\hat{V}_t = 0.7$ [6]. (b) Variation of the dimensionless macroscopic diffusion coefficient versus inclination angle β, for various Atwood numbers At. The fitted curve shown is also suggested by Ref. [23] which is given by Eq. (A2).

stationary mixing core and use $\hat{x}/\sqrt{\hat{t}}$ as a similarity parameter [23]. Thus, flow is controlled by a linear diffusion equation,

$$\frac{\partial \bar{C}}{\partial \hat{t}} = \hat{D}_M \frac{\partial^2 \bar{C}}{\partial \hat{x}^2}. \tag{A1}$$

Here, $\hat{D}_M$ is a *macroscopic* diffusion coefficient which may be $O(10^5)$ greater than the molecular diffusivity $\hat{D}_m$, and is determined by fitting the averaged concentration profile $\bar{C}(\hat{x}, \hat{t})$, to solutions of Eq. (A1). Our measured $\hat{D}_M$ for diffusive experiments in Fig. 15(b) obey the expression proposed by Seon *et al.* (2007) [23],

$$\frac{\hat{D}_M \mathrm{Re}_t^{3/2}}{\hat{V}_t \hat{D}} = 5 \times 10^3 \, (1 + 3.6 \tan\beta)^2, \tag{A2}$$

for $\mathrm{Re}_t \lesssim 1000$, which covers the range of our pure exchange experiments. Note that the macroscopic diffusion coefficient measurements in Fig. 15(b) agree with Eq. (A2), with deviations of comparable magnitude to those reported in Refs. [23,37].

[1] T. B. Benjamin, Gravity currents and related phenomena, J. Fluid Mech. **31**, 209 (1968).
[2] J. O. Shin, S. B. Dalziel, and P. F. Linden, Gravity currents produced by lock exchange, J. Fluid Mech. **521**, 1 (2004).
[3] V. K. Birman, B. A. Battandier, E. Meiburg, and P. F. Linden, Lock-exchange flows in sloping channels, J. Fluid Mech. **577**, 53 (2007).
[4] M. H. I. Baird, K. Aravamudan, N. V. R. Rao, J. Chadam, and A. P. Peirce, Unsteady axial mixing by natural convection in vertical column, AIChE J. **38**, 1825 (1992).
[5] H. R. C. Pratt and M. H. I. Baird, Axial dispersion, in *Handbook of Solvent Extraction*, edited by T. C. Lo, M. H. I. Baird, and C. Hanson (Wiley, New York, 1983).

[6] T. Seon, J. P. Hulin, D. Salin, B. Perrin, and E. J. Hinch, Buoyancy driven miscible front dynamics in tilted tubes, Phys. Fluids **17**, 031702 (2005).
[7] T. Seon, J. Znaien, D. Salin, J.-P. Hulin, E. J. Hinch, and B. Perrin, Transient buoyancy-driven front dynamics in nearly horizontal tubes, Phys. Fluids **19**, 123603 (2007).
[8] K. Alba, S. M. Taghavi, and I. A. Frigaard, Miscible density-unstable displacement flows in inclined tube, Phys. Fluids **25**, 067101 (2013).
[9] J. W. Rottman and J. E. Simpson, Gravity currents produced by instantaneous releases of a heavy fluid in a rectangular channel, J. Fluid Mech. **135**, 95 (1983).
[10] K. Alba, S. M. Taghavi, and I. A. Frigaard, A weighted residual method for two-layer non-Newtonian channel flows: Steady-state results and their stability, J. Fluid Mech. **731**, 509 (2013).
[11] Z. Borden and E. Meiburg, Circulation-based models for Boussinesq internal bores, J. Fluid Mech. **726**, R1 (2013).
[12] M. A. Khodkar, M. M. Nasr-Azadani, and E. Meiburg, Partial-depth lock-release flows, Phys. Rev. Fluids **2**, 064802 (2017).
[13] K. C. Sahu and S. P. Vanka, A multiphase lattice Boltzmann study of buoyancy-induced mixing in a tilted channel, Comput. Fluids **50**, 199 (2011).
[14] K. Alba, S. M. Taghavi, and I. A. Frigaard, Miscible heavy-light displacement flows in an inclined two-dimensional channel: A numerical approach, Phys. Fluids **26**, 122104 (2014).
[15] Y. Hallez and J. Magnaudet, Buoyancy-induced turbulence in a tilted pipe, J. Fluid Mech. **762**, 435 (2015).
[16] W. D. Hill, R. R. Rothfus, and K. Li, Boundary-enhanced sedimentation due to settling convection, Int. J. Multiphase Flow **3**, 561 (1977).
[17] A. Acrivos and E. Herbolzheimer, Enhanced sedimentation in settling tanks with inclined walls, J. Fluid Mech. **92**, 435 (1979).
[18] E. Herbolzheimer and A. Acrivos, Enhanced sedimentation in narrow tilted channels, J. Fluid Mech. **108**, 485 (1981).
[19] R. T. Bonnecaze, H. E. Huppert, and J. R. Lister, Particle-driven gravity currents, J. Fluid Mech. **250**, 339 (1993).
[20] E. Meiburg and B. Kneller, Turbidity currents and their deposits, Annu. Rev. Fluid Mech. **42**, 135 (2010).
[21] J. Zhou, B. Dupuy, A. L. Bertozzi, and A. E. Hosoi, Theory for Shock Dynamics in Particle-Laden Thin Films, Phys. Rev. Lett. **94**, 117803 (2005).
[22] B. P. Cook, A. L. Bertozzi, and A. E. Hosoi, Shock solutions for particle-laden thin films, SIAM J. Appl. Math. **68**, 760 (2008).
[23] T. Seon, J. Znaien, D. Salin, J.-P. Hulin, E. J. Hinch, and B. Perrin, Front dynamics and macroscopic diffusion in buoyant mixing in a tilted tube, Phys. Fluids **19**, 125105 (2007).
[24] T. Ward, C. Wey, R. Glidden, A. E. Hosoi, and A. L. Bertozzi, Experimental study of gravitation effects in the flow of a particle-laden thin film on an inclined plane, Phys. Fluids **21**, 083305 (2009).
[25] N. Murisic, J. Ho, V. Hu, P. Latterman, T. Koch, K. Lin, M. Mata, and A. L. Bertozzi, Particle-laden viscous thin-film flows on an incline: Experiments compared with a theory based on shear-induced migration and particle settling, Physica D **240**, 1661 (2011).
[26] N. Murisic, B. Pausader, D. Peschka, and A. L. Bertozzi, Dynamics of particle settling and resuspension in viscous liquid films, J. Fluid Mech. **717**, 203 (2013).
[27] R. H. Davis, E. Herbolzheimer, and A. Acrivos, Wave formation and growth during sedimentation in narrow tilted channels, Phys. Fluids **26**, 2055 (1983).
[28] S. Saha, D. Salin, and L. Talon, Low Reynolds number suspension gravity currents, Eur. Phys. J. E **36**, 85 (2013).
[29] N. Mirzaeian and K. Alba, Monodisperse particle-laden exchange flows in a vertical duct, J. Fluid Mech. **847**, 134 (2018).
[30] G. Segre and A. Silberberg, Radial particle displacements in Poiseuille flow of suspensions, Nature **189**, 209 (1961).
[31] J. A. Wiklund, M. Stading, A. J. Pettersson, and A. Rasmuson, A comparative study of UVP and LDA techniques for pulp suspensions in pipe flow, AIChE J. **52**, 484 (2006).

[32] E. B. Nelson and D. Guillot, *Well Cementing* (Schlumberger Educational Services, Sugar Land, Tex, 2006).
[33] A. A. Boateng, *Rotary Kilns: Transport Phenomena and Transport Processes* (Butterworth-Heinemann, London, 2015).
[34] A. K. Asomah and T. J. Napier-Munn, An empirical model of hydrocyclones incorporating angle of cyclone inclination, Miner. Eng. **10**, 339 (1997).
[35] A. M. Hamed, Experimental investigation on the adsorption/desorption processes using solid desiccant in an inclined-fluidized bed, Renew. Energ. **30**, 1913 (2005).
[36] A. Hasnain, E. Segura, and K. Alba, Buoyant displacement flow of immiscible fluids in inclined pipes, J. Fluid Mech. **824**, 661 (2017).
[37] B. Eslami, S. Shariatnia, H. Ghasemi, and K. Alba, Non-isothermal buoyancy-driven exchange flows in inclined pipes, Phys. Fluids **29**, 062108 (2017).
[38] L. Espín and S. Kumar, Forced spreading of films and droplets of colloidal suspensions, J. Fluid Mech. **742**, 495 (2014).
[39] I. M. Krieger, Rheology of monodisperse latices, Adv. Colloid Interface Sci. **3**, 111 (1972).
[40] S. H. Maron and P. E. Pierce, Application of Ree-Eyring generalized flow theory to suspensions of spherical particles, J. Colloid Sci. **11**, 80 (1956).
[41] J. B. Segur and H. E. Oberstar, Viscosity of glycerol and its aqueous solutions, Ind. Eng. Chem. **43**, 2117 (1951).
[42] The criteria for locating fronts are verified by those in previous works of the authors [8,36,37].
[43] J. F. Richardson and W. N. Zaki, The sedimentation of a suspension of uniform spheres under conditions of viscous flow, Chem. Eng. Sci. **3**, 65 (1954).
[44] J. C. Bacri, C. Frenois, M. Hoyos, R. Perzynski, N. Rakotomalala, and D. Salin, Acoustic study of suspension sedimentation, Europhys. Lett. **2**, 123 (1986).
[45] J. Martin, N. Rakotomalala, and D. Salin, Accurate determination of the sedimentation flux of concentrated suspensions, Phys. Fluids **7**, 2510 (1995).
[46] D. Leighton and A. Acrivos, The shear-induced migration of particles in concentrated suspensions, J. Fluid Mech. **181**, 415 (1987).
[47] R. J. Phillips, R. C. Armstrong, R. A. Brown, A. L. Graham, and J. R. Abbott, A constitutive equation for concentrated suspensions that accounts for shear-induced particle migration, Phys. Fluids **4**, 30 (1992).
[48] B. P. Cook, Theory for particle settling and shear-induced migration in thin-film liquid flow, Phys. Rev. E **78**, 045303 (2008).
[49] S. Sridharan and R. I. Cukier, The mutual diffusion coefficient of a fluid in the presence of macroparticles, J. Phys. Chem. **88**, 1237 (1984).
[50] G. D'Errico, O. Ortona, F. Capuano, and V. Vitagliano, Diffusion coefficients for the binary system glycerol + water at 25 C. A velocity correlation study, J. Chem. Eng. Data **49**, 1665 (2004).
[51] S. M. Taghavi, T. Seon, D. M. Martinez, and I. A. Frigaard, Influence of an imposed flow on the stability of a gravity current in a near horizontal duct, Phys. Fluids **22**, 031702 (2010).
[52] R. R. Kerswell, Exchange flow of two immiscible fluids and the principle of maximum flux, J. Fluid Mech. **682**, 132 (2011).
[53] S. Lee, A. Mavromoustaki, G. Urdaneta, K. Huang, and A. L. Bertozzi, Experimental investigation of bidensity slurries on an incline, Granular Matter **16**, 269 (2014).